DESIGN AND EXPERIMENTAL CHARACTERIZATION OF PHOTONIC CRYSTAL BASED OPTICAL MODULATORS

A THESIS SUBMITTED TO
THE GRADUATE SCHOOL OF NATURAL AND APPLIED SCIENCES
OF
MIDDLE EAST TECHNICAL UNIVERSITY

BY

ONUR AKDENIZ

IN PARTIAL FULFILLMENT OF THE REQUIREMENTS
FOR
THE DEGREE OF MASTER OF SCIENCE
IN
ELECTRICAL AND ELECTRONICS ENGINEERING

JUNE 2023

Approval of the thesis:

DESIGN AND EXPERIMENTAL CHARACTERIZATION OF PHOTONIC CRYSTAL BASED OPTICAL MODULATORS

submitted by **ONUR AKDENIZ** in partial fulfillment of the requirements for the degree of **Master of Science in Electrical and Electronics Engineering Department, Middle East Technical University** by,

Prof. Dr. Halil Kalıpçılar
Dean, Graduate School of **Natural and Applied Sciences**

Prof. Dr. İlkay Ulusoy
Head of Department, **Electrical and Electronics Engineering**

Assoc. Prof. Dr. Serdar Kocaman
Supervisor, **Electrical and Electronics Engineering, METU**

Examining Committee Members:

Prof. Dr. Gönül Turhan Sayan
Electrical and Electronics Engineering, METU

Assoc. Prof. Dr. Serdar Kocaman
Electrical and Electronics Engineering, METU

Prof. Dr. Haluk Külah
Electrical and Electronics Engineering, METU

Assist. Prof. Dr. Erdinç Tatar
Electrical and Electronics Engineering, Bilkent University

Assist. Prof. Dr. Ahmet Cemal Durgun
Electrical and Electronics Engineering, METU

Date:23.06.2023

I hereby declare that all information in this document has been obtained and presented in accordance with academic rules and ethical conduct. I also declare that, as required by these rules and conduct, I have fully cited and referenced all material and results that are not original to this work.

Name, Surname: Onur Akdeniz

Signature :

ABSTRACT

DESIGN AND EXPERIMENTAL CHARACTERIZATION OF PHOTONIC CRYSTAL BASED OPTICAL MODULATORS

Akdeniz, Onur
M.S., Department of Electrical and Electronics Engineering
Supervisor: Assoc. Prof. Dr. Serdar Kocaman

June 2023, 65 pages

Photonic crystals are materials where the refractive index changes periodically. Thanks to the formation of photonic bands in specific crystal directions, they are helpful tools to control and manipulate light. The optical phase-shifter lengths can be significantly decreased by utilizing negative refraction phenomena in photonic crystal slabs to create large effective refractive index changes during band-to-band transitions. In this thesis, a silicon optical modulator utilizing negative refraction phenomena was analyzed for improvements in its design and experimentally characterized. The design uses the plasma dispersion effect to create optical carrier injection in one arm of a Mach Zehnder interferometer and achieve modulation. The analysis of the improvements in the design entailed explorations of the impacts of photonic crystal size and lattice structure. The photonic crystal region parameters were optimized to minimize the width of the photonic bandgap, effectively decreasing the optical losses and achieving the required phase changes in the on and off states of the modulator. Moreover, photonic bandgaps were examined through an optical spectrum analyzer, and the optical modulation operation was achieved during the experiments.

Keywords: optical communication systems, Mach Zehnder interferometer, photonic crystals, band to band transition, plasma dispersion effect

ÖZ

FOTONİK KRİSTAL TABANLI OPTİK MODÜLATÖRLERİN TASARIMI VE DENEYSEL KARAKTERİZASYONU

Akdeniz, Onur
Yüksek Lisans, Elektrik ve Elektronik Mühendisliği Bölümü
Tez Yöneticisi: Doç. Dr. Serdar Kocaman

Haziran 2023 , 65 sayfa

Fotonik kristaller kırıcılık indisinin periodik olarak değiştiği malzemelerdir. Belirli kristal yönlerinde oluşan fotonik bant aralıkları sayesinde, ışığın kontrolü ve yönlendirilmesinde yardımcı araçlardır. Optik faz kaydırıcıların uzunlukları, fotonik kristal levhalarda negatif kırılım olayını banttan banda geçişler sırasında büyük efektif kırılma indisi değişiklikleri oluşturmak için kullanarak önemli ölçüde azaltılabilir. Bu tezde, negatif kırıcılık olayını kullanan bir silikon optik modülatör, tasarımın geliştirilmesi için analiz edildi ve deneysel olarak karakterize edildi. Tasarım, Mach Zenhder interferometresinin bir koluna optik taşıyıcıların enjeksiyonu ve modülasyonun gerçekleştirilmesi için plazma dağılım etkisini kullanıyor. Tasarımdaki geliştirilmelere yönelik analiz, fotonik kristal boyutunun ve örgü yapısının etkilerinin incelenmesini gerektirdi. Fotonik kristal bölgesi parametreleri bant aralık genişliğinin azaltılması, bunun sonucunda optik kayıpların azalması ve modülatörün açık ve kapalı durumları için gereken faz farklarına ulaşmak için optimize edildi. Ayrıca, fotonik bant aralıkları optik spektrum analizörü ile incelendi ve deneyler esnasında optik modülasyon operasyonu gerçekleştirildi.

Anahtar Kelimeler: optik haberleşme sistemleri, Mach Zehnder interferometresi, fotonik kristaller, banttan banta geçiş, plazma dağılım etkisi

To my family

ACKNOWLEDGMENTS

First, I would like to express my deepest gratitude to my supervisor Assoc. Dr. Serdar Kocaman for his guidance, advice, criticism, encouragement, and insight throughout the research.

I acknowledge the financial support of the TUBITAK BIDEB 2210-A 2020/2 Scholarship Program during this study.

I thank to Prof. Dr. Gönül Turhan Sayan, Prof. Dr. Haluk Külah, Assist. Prof. Dr. Ahmet Cemal Durgun, and Assist. Prof. Dr. Erdinç Tatar for being on my thesis committee.

I want to thank Alper Şahin for supporting and contributing to this work, Utku Yılmaz for providing my initial training on the experimental setup in our laboratory, and Yalın Başay for accompanying me in my latest experiments. I also want to thank Ozan Berk Boyraz for his support and friendship.

Lastly, I am grateful to my mother, father, and sister for always supporting and motivating me in my studies and life.

TABLE OF CONTENTS

ABSTRACT v

ÖZ vii

ACKNOWLEDGMENTS x

TABLE OF CONTENTS xi

LIST OF TABLES xiii

LIST OF FIGURES xiv

LIST OF ABBREVIATIONS xviii

CHAPTERS

1 INTRODUCTION 1

1.1 Optical Communication Systems 1

1.1.1 Properties of Silicon As An Optical Material 3

1.1.2 Components of Optical Communication Systems 4

1.2 Modulators 6

1.2.1 Modulation Methods 6

1.2.1.1 Pockels and Kerr’s Effects 6

1.2.1.2 Franz-Keldysh Effect 7

1.2.1.3 Thermal Modulation 7

1.2.1.4 Plasma Dispersion Effect 8

1.2.2 Modulator Types 9

2 PHOTONIC CRYSTALS 13

2.1 Electromagnetic Background 13

2.2 Photonic Band Formation 15

2.3 Photonic Crystal Slabs 18

2.4 Band-to-Band Transition Mechanism 21

3 MODULATOR DESIGN 23

3.1 Overview of Modulator Operation 23

3.2 Design of Photonic Crystal Region 24

3.2.1 Bandgap Optimization 24

3.2.2 Phase Difference Calculations 27

3.3 Design of PIN Diode 34

4 RESULTS AND DISCUSSIONS 39

4.1 Fabrication and SEM Imaging 39

4.2 Experimental Characterization of Modulator 44

4.2.1 Photonic Bandgap Measurements 46

4.2.2 Verification of P-I-N Diode Operation 49

4.2.3 Modulation Experiments 49

5 CONCLUSION AND FUTURE WORK 57

REFERENCES 61

LIST OF TABLES

TABLES

Table 3.1 The optical path difference/wavelength calculated using Equation 3.2, for $a = 550\ nm$ and $D = 350\ nm$. 33

Table 3.2 The optical path difference/wavelength calculated using Equation 3.16. 33

Table 3.3 The optical path difference/wavelength calculated using Equation 3.17. 34

Table 4.1 Bandgap centers (BGCs) and bandgap widths (BGWs) of photonic crystals with Γ - M direction at designed and fabricated sizes, based on MPB simulations. 44

Table 4.2 Bandgap centers and bandgap widths of photonic crystals with Γ - K direction at designed and fabricated sizes, based on MPB simulations. . 44

Table 4.3 The measured bandgap centers and bandgap widths of photonic crystals with Γ - M direction with varying hole sizes. 46

LIST OF FIGURES

FIGURES

Figure 1.1 The international bandwidth usage from 2017 to 2022 [7, 8], and its projection for the next two years. 2

Figure 1.2 The attenuation coefficient $\alpha(dB/km)$ and the dispersion coefficient D_λ $(ps/km - nm)$ of fused silica glass fibers [2]. 3

Figure 1.3 A simple diagram for an optical communication system. Redrawn after [12]. 4

Figure 1.4 A simple diagram for an optical communication system. Redrawn after [1]. 5

Figure 1.5 The bending of bands (a) and change of absorption coefficient (b) under external electric field in a bulk semiconductor [2]. 8

Figure 1.6 Simple diagram of an MZI [2]. 9

Figure 1.7 Interference of two waves of equal intensity for varying phase difference. 10

Figure 2.1 Picture of reflection and refraction for a flat surface in ray optics. Redrawn after [22]. 15

Figure 2.2 Parallel wave vector $k_{||}$ vs. frequency w, for a plane of glass with the finite thickness (a) [22]. 16

Figure 2.3 A dielectric structure with discrete translational symmetry in the y direction. Redrawn after [22]. 17

Figure 2.4 The irreducible Brillouin zone for 2D photonic crystals. 19

Figure 2.5 Band diagrams of photonic crystal slabs. Calculated via MPB. . 20

Figure 2.6 TM bands for hexagonal lattice photonic crystals at the direction of Γ - M. 21

Figure 3.1 Summary of the operation mechanism of the modulator design [13]. 23

Figure 3.2 Band diagram for hexagonal lattice photonic crystals with hole diameters of 350 nm and period of 550 nm. 25

Figure 3.3 TE & TM gaps for $a = 550\ nm$ at Γ - M direction. 25

Figure 3.4 TE & TM gaps, for photonic crystals at Γ - M direction. 27

Figure 3.5 Band diagram for hexagonal lattice photonic crystals with hole diameters of 280 nm and period of 550 nm. 28

Figure 3.6 TE & TM gaps for $a = 550\ nm$ at Γ - K direction. 28

Figure 3.7 TE & TM gaps, for photonic crystals at Γ - K direction. 29

Figure 3.8 An arbitrary wavelength vs. wave vector graph for V_{ON} and V_{OFF}. 30

Figure 3.9 The shift of TM bands for hexagonal lattice photonic crystals with a period of 550 nm and hole diameter of 350 nm at the direction of Γ - K for varying silicon refractive index. 31

Figure 3.10 The lattice diagram for position and reciprocal spaces. Redrawn after [22]. 32

Figure 3.11 PIN diode, MZI active region, and their cross-section. 35

Figure 3.12 Doping concentration for varying silicon depths. 35

Figure 3.13 Carrier concentrations under no bias voltage in the active region for silicon depth varying from 10 nm to 250 nm. 36

Figure 3.14 Electron concentration under bias voltage in the active region for silicon depth varying from 10 nm to 250 nm when 85 μA current passes through the diode. 36

Figure 3.15 Hole concentration under bias voltage in the active region for silicon depth varying from 10 nm to 250 nm when 85 μA current passes through the diode. 37

Figure 3.16 Change of refractive index of silicon in the active region for silicon depth varying from 10 nm to 250 nm when 85 μA current passes through the diode. 37

Figure 4.1 Waveguide with PhCs at Γ - M direction. 40

Figure 4.2 Waveguide with PhCs at Γ - K direction. 40

Figure 4.3 MZI active region with PhCs at Γ - M direction. 41

Figure 4.4 MZI active region with PhCs at Γ - K direction with side holes at Γ - M direction. 41

Figure 4.5 SEM imaging of photonic crystals with 310 nm design diameter at Γ - M direction (Sample 1). 42

Figure 4.6 Photonic crystal size: design vs fabrication (Sample 1). 43

Figure 4.7 Photonic crystal period: design vs. fabrication (Sample 1). . . . 43

Figure 4.8 The photo of the experimental setup. 45

Figure 4.9 The diagram of the experimental setup. 45

Figure 4.10 The normalized spectrum of Γ - M photonic crystal waveguides with N=120. 47

Figure 4.11 The normalized spectrum of Γ - K photonic crystal waveguides with N=120. 48

Figure 4.12 Current-voltage characteristics of PIN diodes. 50

Figure 4.13 Thorlabs DET10N/M, response to 20kHz impulse. 51

Figure 4.14 Thorlabs DXM30AF, response to 20kHz impulse. 51

Figure 4.15 Modulation at 1550 nm, for Device 1. 53

Figure 4.16 Single-sided PSD of Device 1 while applying ± 5 V square wave. 54

Figure 4.17 Spectrum of Device 2 while applying 10 V DC voltage. 55

LIST OF ABBREVIATIONS

5G	5^{th} generation
CMOS	complementary metal oxide semiconductor
WDM	wavelength division multiplexing
LED	light-emitting diodes
EMI	electromagnetic interference
AM	amplitude modulation
PM	phase modulation
FM	frequency modulation
MZI	Mach Zehnder interferometer
PhC	photonic crystal
2D	2 dimensional
TE	transverse electric
TM	transverse magnetic
SOI	silicon on insulator
RIE	reactive ion etching
SEM	scanning electron microscope
OSA	optical spectrum analyzer
BGC	bandgap center
BGW	bandgap width
PSD	power spectral density

CHAPTER 1

INTRODUCTION

Photonic crystals are materials with periodically changing refractive indices. Similar to the formation of electronic bands in crystalline materials, photonic crystals give rise to the formation of photonic bands. By engineering these photonic bands, light propagation can be manipulated for photonic applications.

The negative refraction phenomena can be utilized in photonic crystal slabs to create significant effective refractive index changes during band-to-band transitions, considerably reducing the phase-shifter length. This master's thesis focuses on improving the design of active photonic crystal regions of a silicon optical modulator by exploring the band structures of photonic crystals and experimental characterization of the designed modulator.

The thesis is organized into five chapters as follows: In Chapter 1, the basics of communication systems and modulators are introduced. In Chapter 2, the formation of photonic bandgaps in photonic crystal structures is analyzed. In Chapter 3, the design of the photonic crystal based optical modulator is explained. In Chapter 4, the experimental characterization of the designed modulator is presented. In Chapter 5, the thesis concludes with discussions on further studies.

1.1 Optical Communication Systems

The increasing growth of internet-based applications, social networking, cloud services, and the latest emerging 5^{th} generation (5G) wireless systems lead to the need for advancements in the transmission capacity of communication systems, data centers, computers, and smartphones [1, 2, 3, 4, 5, 6]. The international bandwidth usage between 2015 and 2022 is illustrated in Figure 1.1, which raised from 156 terabits per second in 2015 to 1230 terabits per second in 2022 [7, 8], and it is expected to reach 1941 terabits per second in 2024 at its current increase rate.

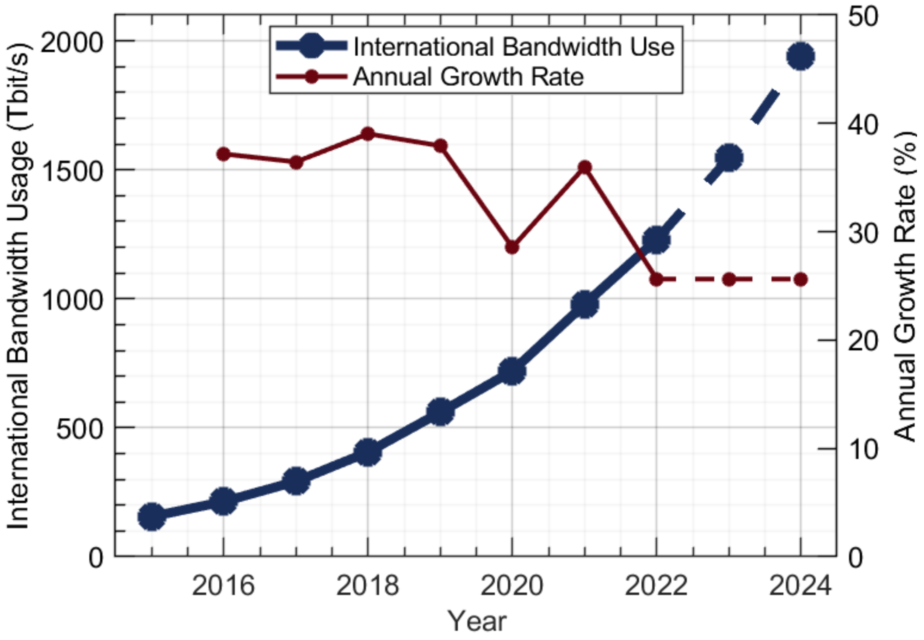

Figure 1.1: The international bandwidth usage from 2017 to 2022 [7, 8], and its projection for the next two years.

The majority of communication systems depended on electrical cables for the transmission of information till the advancements in compact and efficient light sources and low-loss optical fibers in the late 1970s [1, 2]. Over the last five decades, silicon-based microelectronic technology has developed as the speed and size of the transistors improved per Moore's law [6, 9]. However, as Moore's law and the copper-based traditional transmission technology approach their limit, the increasing demands for high speed and large bandwidth cannot be satisfied [6, 9]. Thanks to their high speed, large bandwidth, and low noise properties, photonic devices are expected to provide low-cost, high-performance solutions to communication systems [6, 9, 10].

1.1.1 Properties of Silicon As An Optical Material

The maturity of the silicon based complementary metal oxide semiconductor (CMOS) industry makes silicon an ideal material for photonic devices and more suitable for massive and low-cost production of the photonic and electronic integrated systems compared to other semiconductors [3, 6, 10, 11].

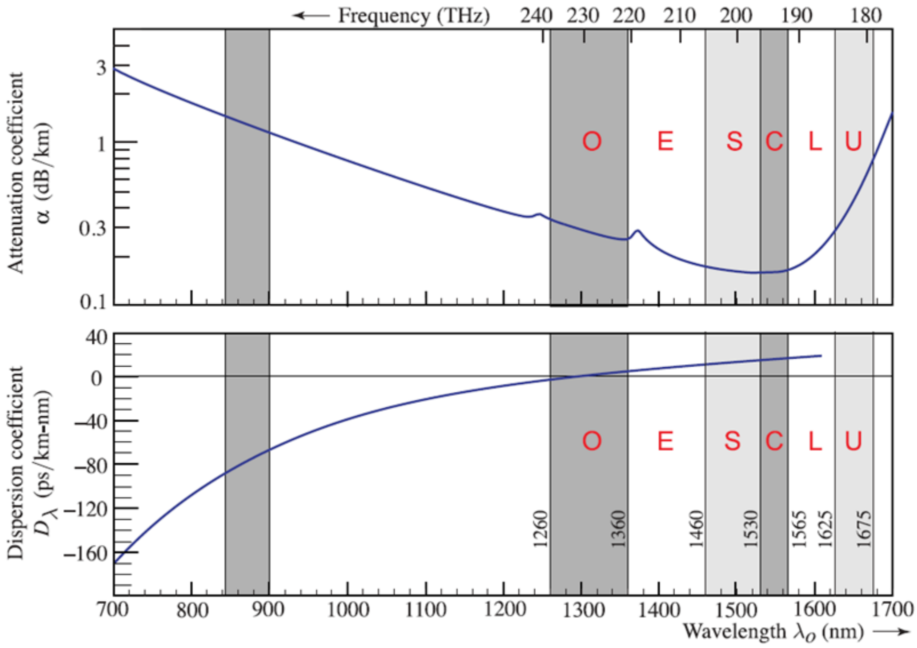

Figure 1.2: The attenuation coefficient $\alpha(dB/km)$ and the dispersion coefficient D_λ $(ps/km-nm)$ of fused silica glass fibers [2].

The attenuation and dispersion coefficients of fused silica glass fibers are given in Figure 1.2 for a spectrum ranging from 700 nm to 1700 nm. In this figure, the labels O, E, S, C, L, and U stand for original, extended, short, conventional, long, and ultra-long bands, respectively. The dark-shaded regions represent the telecommunications bands. The first telecommunication systems used the band centered at 870 nm. The O band is centered at 1310 nm, where the dispersion is lowest, while the C band is centered at 1550 nm, where the attenuation is lowest. The other bands (E, S, L, and U) are used in various wavelength division multiplexing (WDM) systems [2].

Based on the attenuation and dispersion characteristics of the silicon, 1.31 and 1.55 µm are the most commonly used bands in fiber optic communication systems [3, 6, 9].

1.1.2 Components of Optical Communication Systems

The purpose of communication systems is to transmit a signal from an information source (computer, telephone, video device, etc.) to the destination through a transmission medium with a high degree of accuracy and reliability. Such a system consists of a transmitter or a modulator on the information source side and a receiver or demodulator at the destination point [1, 12]. A simple diagram for a general communication system is given in Figure 1.3.

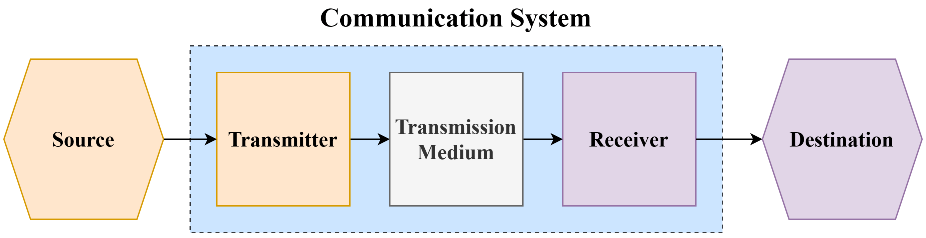

Figure 1.3: A simple diagram for an optical communication system. Redrawn after [12].

In electrical communication systems, the information source feeds an electrical signal to an electronic transmitter. The transmitter transforms the signal to a proper form by modulating a carrier which then propagates over the transmission medium. The transmitting medium could be a pair of wires, a coaxial cable, or a radio link through free space. In the case of long-haul systems, it is necessary to install repeaters and line amplifiers at intervals to cope with attenuation and distortion. The propagated signal is demodulated at the receiver end to form the original electrical signal and delivered to the destination [12].

In optical fiber communication systems, the transmitter modulates lightwave carriers generated by an optical source. The transmitting medium is optical fiber cables. Again, optical amplifiers are employed in long-distance systems to overcome the effects of attenuation and distortion. At the receiver end, the propagating optical carriers are demodulated and transformed to electrical signals by an optical detector, which can be a photodiode, a phototransistor, or a photoconductor [1, 12]. A simple diagram for an optical fiber communication system is given in Figure 1.4.

The optical fibers are cylindrical dielectric waveguides providing a medium to prop-

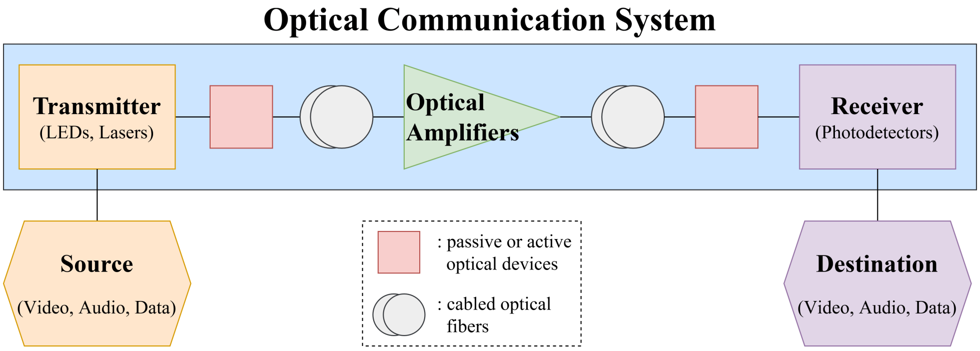

Figure 1.4: A simple diagram for an optical communication system. Redrawn after [1].

agate and direct the lightwave carriers along the direction of their axis. They are usually made of fused silica glass (SiO_2) and can be packed with copper wires to energize optical amplifiers in long-haul systems [1, 2].

The lightwave carriers are sent into the fiber by a transmitter. The possible light sources for transmitters are semiconductor light-emitting diodes (LEDs) and laser diodes. The output light of these sources can be modulated by changing their input currents at the desired rate, which is called direct modulation. For applications requiring rates higher than 2.5 Gb/s, an external modulation is preferred [1].

Optical amplifiers are employed in long-distance systems to overcome the effects of attenuation and distortion due to scattering, absorption, and dispersion of light in the fiber. They can be used as post amplifiers after the transmitter to boost the optical power inputted to fiber, line amplifiers to preserve the optical power through transmission, and preamplifiers before the receiver to produce gain. The erbium-doped fiber amplifiers (EDFAs), rare-earth doped fiber amplifiers (REFAs), and Raman fiber amplifiers (RFAs) are examples of optical fiber amplifiers used in optical fiber communication systems [1, 2].

A photodetector converts the optical power to an electrical signal (photocurrent) at the receiver end. The p-i-n (PIN) photodiodes with their large bandwidth and avalanche photodiodes (APDs) with their gain mechanism are the most common photodetectors used in optical fiber communication systems [1, 2].

Compared to electrical communication systems, optical fiber communication systems have advantages such as greater bandwidth potential, immunity to electromagnetic interference (EMI) and crosstalk, lower system size, propagation loss, and potential cost [1, 2].

1.2 Modulators

Optical modulators are essential for optical communication, thermal sensing, and imaging systems [11]. Their primary function is to modulate optical signals by altering their amplitude, phase, or frequency to achieve amplitude modulation (AM), phase modulation (PM), or frequency modulation (FM) [2, 13].

1.2.1 Modulation Methods

The most common modulation methods are the use of linear electro-optical effect (Pockels effect), quadratic electro-optical effect (Kerr effect), Franz-Keldysh effect, thermo-optical effect, and free carrier plasma dispersion effect [11, 13, 14]. These methods are briefly explained in the following subsections.

1.2.1.1 Pockels and Kerr's Effects

The Pockels effect and Kerr effect are based on the change in the dielectric function of the material with the applied electric field [11, 13].

The refractive index (n) of electro-optic mediums can be expressed as a function of the magnitude of the applied electric field (E) as in Equation 1.1[2].

$$n\left(E\right) \approx n + a_1 E + \frac{1}{2} a_2 E^2 + \ldots \tag{1.1}$$

Here, the terms n, a_1, and a_2 are expressed as:

$$n = n(0), a_1 = \left.\frac{dn}{dE}\right|_{E=0}, a_2 = \left.\frac{d^2 n}{dE^2}\right|_{E=0} \tag{1.2}$$

By rearranging the terms, we can rewrite the expression for the refractive index as in Equation 1.3 [2].

$$n\left(E\right) \approx n - \frac{1}{2}rn^3E - \frac{1}{2}sn^3E^2 + \ldots \tag{1.3}$$

Here, the terms r and s are defined as:

$$r = \frac{-2a_1}{n^3}, s = \frac{-2a_2}{n^3} \tag{1.4}$$

If the refractive index of an electro-optic medium changes linearly with the applied electric field as in Equation 1.5, the medium is called a Pockels medium, the coefficient r is called the Pockels coefficient, and the change of refractive index is called as the Pockels effect [2]. The intrinsic silicon exhibits a weak Pockels effect due to its centrosymmetric structure [11].

$$n\left(E\right) \approx n - \frac{1}{2}rn^3E \tag{1.5}$$

If the refractive index of an electro-optic medium changes quadratically with the applied electric field as in Equation 1.6, the medium is called a Kerr medium, the coefficient s is called the Kerr coefficient, and the change of refractive index is called as the Kerr effect [2]. The Kerr effect in silicon is not strong enough to produce high refractive index change[13].

$$n\left(E\right) \approx n - \frac{1}{2}rn^3E \tag{1.6}$$

1.2.1.2 Franz-Keldysh Effect

The Franz-Keldysh effect is a shift of the absorption spectrum to longer wavelengths due to the extension of the absorption edge into the forbidden gap via an external electrical field. It is illustrated in Figure 1.5 [2].

The Franz-Keldysh effect is not strong enough to produce a high refractive index change in silicon [13].

1.2.1.3 Thermal Modulation

The thermo-optical effect is based on the change in the dielectric function of the material with the temperature variation. Although silicon has a high thermo-optic co-

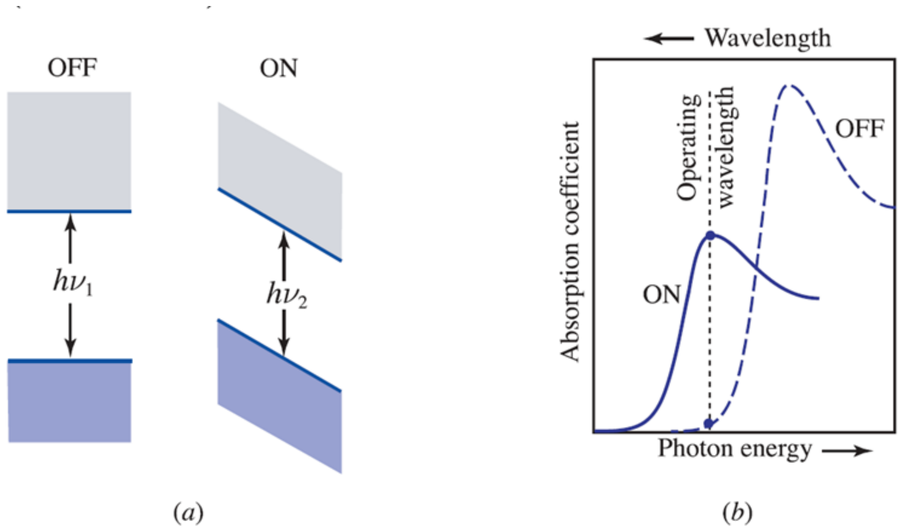

Figure 1.5: The bending of bands (a) and change of absorption coefficient (b) under external electric field in a bulk semiconductor [2].

efficient, thermo-optic modulation has a slow response time and requires high power, thus unsuitable for optical communication [11, 13].

1.2.1.4 Plasma Dispersion Effect

The free carrier plasma dispersion effect is based on the change in the dielectric function of the material with free carrier concentration. The free carrier concentration may be adjusted via injection, depletion, or accumulation of the carriers. This modulation method provides high spectral modulation depth and speed [11, 13, 14].

The formula describing the variation of refractive index (Δn) considering the concentration of free electrons (ΔN_e) and holes (ΔN_h) is given in Equation 1.7 [15].

$$\Delta n = \frac{e^3\,\lambda^2}{8\pi^2\,c^3\,\epsilon_0\,n}\left(\frac{\Delta N_e}{m^*_{ce}} + \frac{\Delta N_h}{m^*_{ch}}\right) \tag{1.7}$$

Here, the terms λ, c, ϵ_0, m^*_{ce}, m^*_{ch} represent wavelength, speed of light in free space, free space permittivity, conductivity effective mass of electrons, and conductivity effective mass of holes.

At the wavelength of 1.55 μm, Equation 1.7 can be expressed more simply, as in Equation 1.8 [16], where Δn_e and Δn_h stand for the change of refractive index due to free electrons and free holes, respectively.

$$\Delta n = \Delta n_e + \Delta n_h = -[8.8 * 10^{-22} \Delta N_e + 8.5 * 10^{-18} (\Delta N_h)^{0.8}] \tag{1.8}$$

1.2.2 Modulator Types

The Mach Zehnder interferometers (MZIs) and resonant structures are two common modulator types.

In the MZIs, the refractive index change at one arm creates constructive or destructive interference at the output. The MZI structures have high speed, a broad working spectrum, and low temperature dependency. However, they require a long interaction length, which increases insertion loss, system area, and power consumption [10, 13, 17, 18, 19].

The resonant structures are alternatives to MZIs, where ring resonators are the most popular resonator form for modulation purposes. Changing the refractive index in the active region causes the resonant wavelength to change, and modulation can be achieved. The ring resonators have lower system area and power consumption. However, they are more sensitive to variations in temperature and process due to their narrow operation range [13, 19, 20, 21].

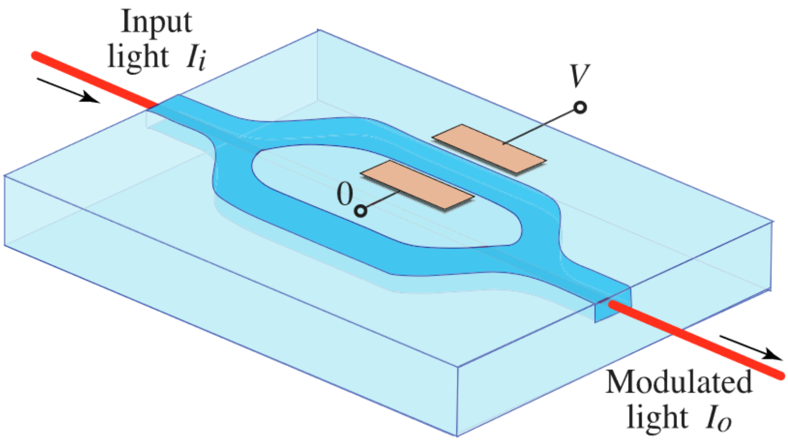

Figure 1.6: Simple diagram of an MZI [2].

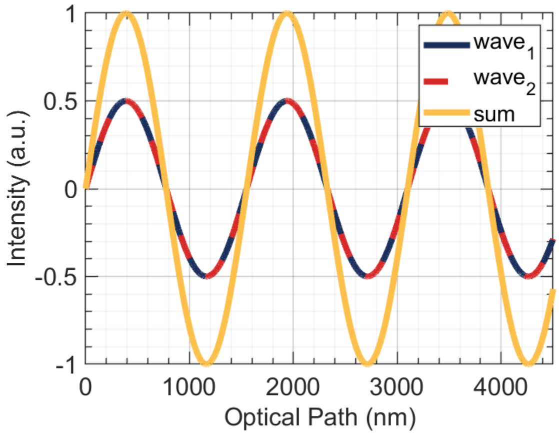

(a) Constructive interference, $\theta = 2\pi n$

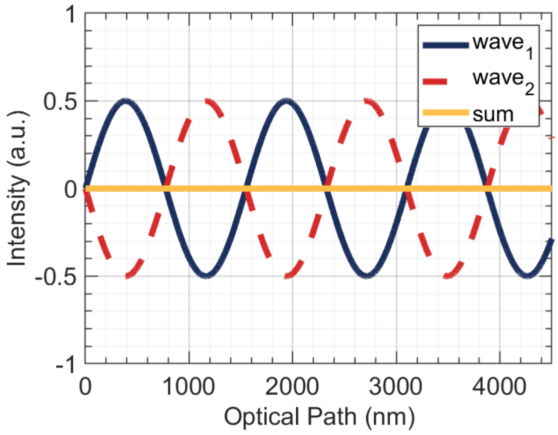

(b) Destructive interference, $\theta = 2\pi(n - \frac{1}{2})$.

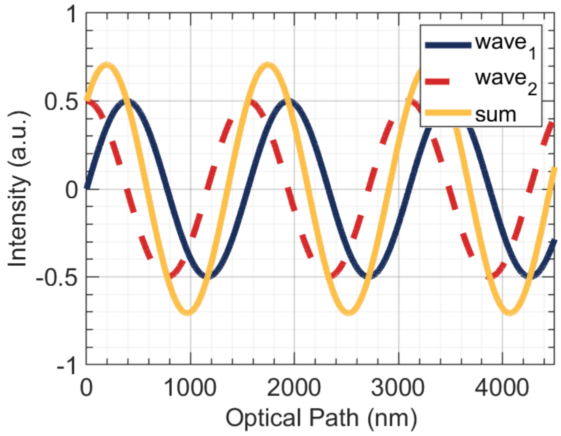

(c) Partial interference, $\theta = 2\pi(n - \frac{1}{4})$.

Figure 1.7: Interference of two waves of equal intensity for varying phase difference.

A simple MZI structure with an electric field applied to one of its arms is given in Figure 1.6. Assuming that the arms of the MZI are identical, the intensity of light transmitted to the output port (I_o) can be expressed as the function of the phase difference (θ) between its arms and the intensity of the light inputted (I_i):

$$I_o = 1/2\ I_i + 1/2\ I_i \cos(\varphi) = I_i \cos^2(\varphi/2) \tag{1.9}$$

Based on Equation 1.9, for integer n, creating a phase difference $\theta = 2\pi n$ would lead to a total constructive interference, while a phase difference of $\theta = 2\pi(n - \frac{1}{2})$ would generate a total destructive interference. For other phase differences, the waves would generate partial interference. These three cases are illustrated in Figure 1.7

In MZIs and ring resonators; PN, PIN diodes, and MOS structures embedded into the optical region can deplete or accumulate free carriers to change the refractive index, inducing constructive or destructive interference.

CHAPTER 2

PHOTONIC CRYSTALS

The photonic crystals are arrays of materials where the dielectric function of media changes periodically. They provide a method for controlling and manipulating light by restricting its propagation in a specific crystal direction for a range of frequencies. These frequency ranges are called photonic bandgaps [22, 23, 24].

2.1 Electromagnetic Background

Maxwell's equations describe the propagation of electromagnetic waves mathematically. These equations are given in Equations 2.1-2.4 in their differential forms.

$$\nabla \cdot \vec{B} = 0 \tag{2.1}$$

$$\nabla \times \vec{E} + \frac{\partial \vec{B}}{\partial t} = 0 \tag{2.2}$$

$$\nabla \cdot \vec{D} = \rho \tag{2.3}$$

$$\nabla \times \vec{H} - \frac{\partial \vec{D}}{\partial t} = \vec{J} \tag{2.4}$$

Here, $\vec{B}$, $\vec{E}$, $\vec{D}$, $\vec{H}$, ρ, and $\vec{J}$ stand for magnetic flux density, electric field intensity, electric flux density (electric displacement), magnetic field intensity, free charge density, and current density, respectively.

Assuming that we are working with small field strengths (linear regime) in a source-free ($\rho = 0$ and $\vec{J} = 0$), macroscopic and isotropic material with real, positive, and material dispersion-free dielectric function, we have constitutive relations, given in Equations 2.5 and 2.6 [22].

$$\vec{D}\left(r\right) = \varepsilon_0 \varepsilon\left(r\right) \vec{E}\left(r\right) \tag{2.5}$$

$$\vec{B}\left(r\right)=\mu_0\mu\left(r\right)\vec{H}\left(r\right) \tag{2.6}$$

Here, r, ε_0, $\varepsilon\left(r\right)$, μ_0, and $\mu\left(r\right)$ stand for position vector, free space permittivity (equal to $8.854 * 10^{-12} Farad/m$), relative permittivity, free space permeability (equal to $4\pi * 10^{-7} Henry/m$), and relative permeability, respectively.

The relative permeability is close to 1 for most dielectric materials, and Equation 2.6 can be simplified as in Equation 2.7.

$$\vec{B}\left(r\right)=\mu_0\vec{H}\left(r\right) \tag{2.7}$$

Inserting constitutive relations given in Equations 2.5 and 2.7 into the Maxwell's equations given in Equations 2.1,2.2, 2.3, and 2.4, they take the following form:

$$\nabla\cdot\vec{H}\left(r,t\right)=0 \tag{2.8}$$

$$\nabla\times\vec{E}\left(r,t\right)+\mu_0\frac{\partial\vec{H}\left(r,t\right)}{\partial t}=0 \tag{2.9}$$

$$\nabla\cdot\left[\varepsilon\left(r\right)\vec{E}\left(r,t\right)\right]=0 \tag{2.10}$$

$$\nabla\times\vec{H}\left(r,t\right)-\varepsilon_0\epsilon\left(r\right)\frac{\partial\vec{E}\left(r,t\right)}{\partial t}=0 \tag{2.11}$$

Since Maxwell's equations are linear, the fields $\vec{E}$ and $\vec{H}$ can be decomposed into their time and space components and expanded into harmonic modes, and $\vec{H}$ can be decomposed into their time and space components and expanded into harmonic modes. These harmonic modes can be expressed as a multiplication of spatial mode profile and a complex exponential function of frequency (w) and time (t), as in Equations 2.12 and 2.13.

$$\vec{H}\left(r,t\right)=\vec{H}\left(r\right)e^{-iwt} \tag{2.12}$$

$$\vec{E}\left(r,t\right)=\vec{E}\left(r\right)e^{-iwt} \tag{2.13}$$

Inserting those field expressions into Maxwell's equations given in Equations 2.8-2.11, we reach Equations 2.14-2.17.

$$\nabla\cdot\vec{H}(r)=0 \tag{2.14}$$

$$\nabla\cdot\left[\varepsilon\left(r\right)\vec{E}\left(r\right)\right]=0 \tag{2.15}$$

$$\nabla\times\vec{E}\left(r\right)-iw\mu_0\vec{H}\left(r\right)=0 \tag{2.16}$$

$$\nabla \times \vec{H}\left(r\right) + iw\varepsilon_0\varepsilon\left(r\right)\vec{E}\left(r\right) = 0 \tag{2.17}$$

The Equations 2.14 and 2.15 require that the fields are made up of transverse electromagnetic waves [22]. Decoupling the Equations 2.16 and 2.17 leads to Equations 2.18 and 2.19.

$$\nabla \times \left[\frac{1}{\varepsilon(r)}\nabla \times \ \vec{H}\left(r\right)\right] = \left(\frac{w}{c}\right)^2 \vec{H}\left(r\right) \tag{2.18}$$

$$\nabla \times \nabla \times \ \vec{E}\left(r\right) = \varepsilon(r)\left(\frac{w}{c}\right)^2 \vec{E}\left(r\right) \tag{2.19}$$

The Equations 2.16 and 2.17 can be rewritten as:

$$\vec{H}\left(r\right) = \frac{-i}{w\mu_0}\nabla \times \vec{E}\left(r\right) \tag{2.20}$$

$$\vec{E}\left(r\right) = \frac{i}{w\varepsilon_o\varepsilon\left(r\right)}\nabla \times \vec{H}\left(r\right) \tag{2.21}$$

The $\vec{E}$ and $\vec{H}$ fields can be obtained by solving either Equations 2.18 and 2.23, or Equations 2.19 and 2.20 simultaneously.

2.2 Photonic Band Formation

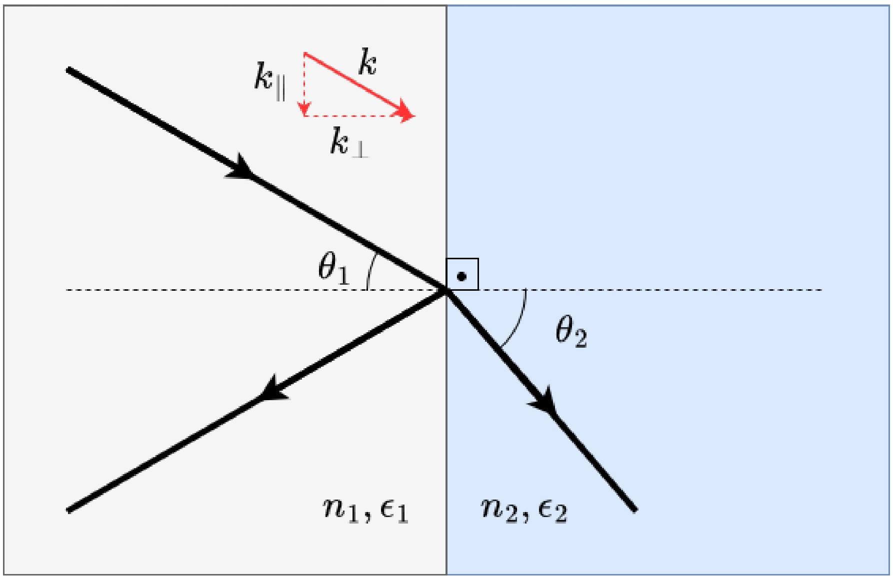

Figure 2.1: Picture of reflection and refraction for a flat surface in ray optics. Redrawn after [22].

The reflection and refraction of light incident to a flat surface from a high dielectric constant (ϵ_1) medium with θ_1 to a low dielectric constant (ϵ_2) medium with θ_2 are pictured, according to ray optics, in Figure 2.1. Here, $k_{||}$and $k_\perp$ are components of wave vector $\vec{k}$ parallel and normal to the interface between two mediums, respectively.

According to ray optics, the incident light with an angle θ_1 greater than the critical angle $\theta_c = \sin^{-1}\left(\frac{n_2}{n_1}\right)$ leads to $\sin\left(\theta_2\right) > 1$. Therefore, there is no real solution, and the incident ray is totally reflected.

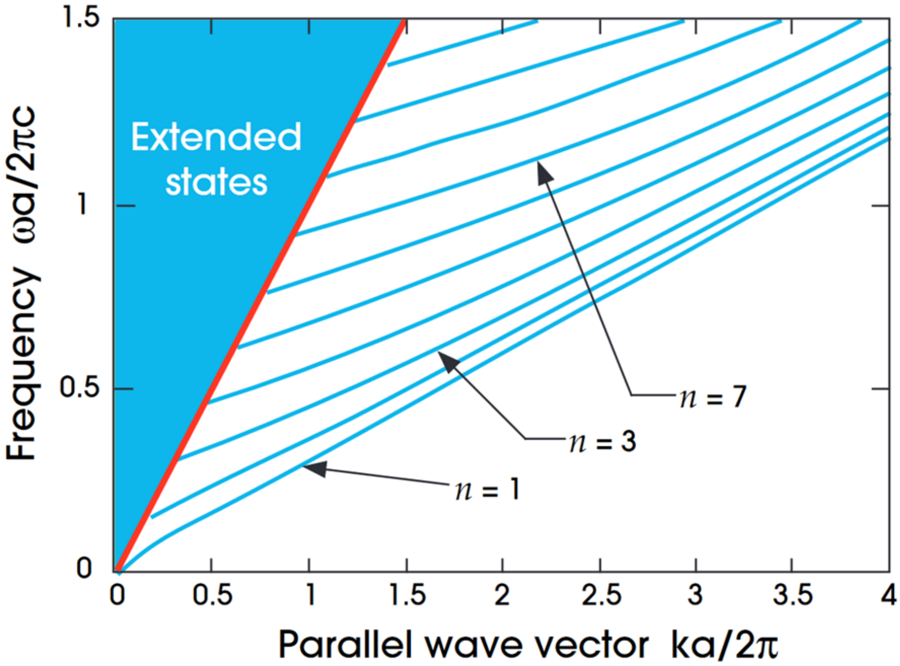

Figure 2.2: Parallel wave vector $k_{||}$ vs. frequency w, for a plane of glass with the finite thickness (a) [22].

The electromagnetic modes in a plane of glass with the finite thickness (a) surrounded by air are not confined to the glass region and extend into the air. These extended waves are the superposition of plane waves with:

$$w = c\,|k| = c\left(k_{||}^2 + k_\perp^2\right)^{1/2}. \tag{2.22}$$

The $w = ck_{||}$ line is called the light line. Since $k_\perp$ can take any value for these extended waves, the modes above the light line, i.e., modes with frequencies greater than c$k_{||}$ can propagate in the air surrounding the glass. This region is called the light cone, and the modes in this region satisfy Snell's law. [22]

In addition to the modes in the light cone, some modes lie below the light line. The perpendicular components ($k_\perp = \pm i\left(k_{||}^2 - \frac{w^2}{c^2}\right)^2$) of the wave vector of these modes are imaginary, meaning they are localized in the glass region and decay exponentially in the air surrounding it. These modes are called index guiding modes and propagate at discrete frequencies for a given $k_{\|}$. These index guiding modes, light line, and light cone for a plane of glass are illustrated in Figure 2.2 [22].

Symmetries in a dielectric structure provide a suitable frame to classify electromagnetic modes of the system. The continuous and discrete translational symmetries are fundamental in periodic dielectric structures such as photonic crystals [22].

A system with continuous translational symmetry remains unchanged after translating through a particular direction for any distance. On the other hand, a system with discrete translational symmetry remains the same after applying a translation through a particular direction for multiples of a fixed step size. This fixed step size is called as the lattice constant (a), and the translation vector in that specific direction with a length of a is called as the primitive lattice vector [22].

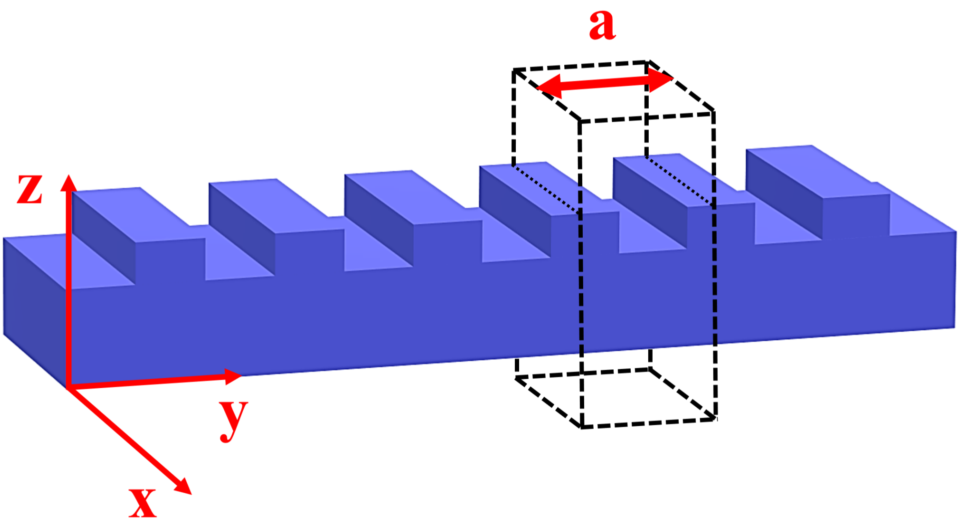

Figure 2.3: A dielectric structure with discrete translational symmetry in the y direction. Redrawn after [22].

A structure with discrete translational symmetry in the y direction is illustrated in Figure 2.3. This structure is formed by repeating the dielectric function given in the rectangular box. This repeating unit is called as the unit cell [22].

The electromagnetic modes in structures with discrete translational symmetry are periodic in the direction of the lattice vector. This is known as Bloch's theorem, and it can be expressed as in Equation 2.23 for the structure in Figure 2.3.

$$H(\ldots,\ y,\ \ldots) \propto e^{(ik_y\ y)}\ u_{k_y}\ \ (y, \ldots) \tag{2.23}$$

Here, u_{k_y} is a periodic function of y with:

$$u_{k_y}\ (y + la, z) = u_{k_y}\ (y, z) \tag{2.24}$$

One result of Bloch's theorem is the periodicity in the mode frequencies $w(k_y)$:

$$w(k_y) = w(k_y + mb) \tag{2.25}$$

Here, $\vec{b} = b\vec{y}$ is the reciprocal lattice vector with $b = \frac{2\pi}{a}$. Thanks to the periodicity in the mode frequencies, we can reduce the range of k_y to be examined to $-\pi/a < k_y \leq \pi/a$, which is called the Brillouin zone [22].

The rotational symmetry in the lattice structure can lead to redundancies in the Brillouin zone, and the range of examination would further shrink to the irreducible Brillouin zone. The 2D square lattice and hexagonal lattice photonic crystals in the spatial domain are given in Figure 2.4a and Figure 2.4c, and their corresponding irreducible Brillouin zones are highlighted in Figure 2.4b and 2.4d, respectively. Here, the letters Γ, X, M, and K represent different directions in the photonic crystal.

2.3 Photonic Crystal Slabs

The photonic crystals can be one-dimensional (1D) as in a multilayer film, two-dimensional (2D) as in infinitely long dielectric columns, and three-dimensional (3D) as in diamond or face-centered cubic (fcc) lattice. The fourth version of the photonic crystals is called photonic crystal slabs, with finite thickness and 2D periodicity [22].

The photonic crystal slabs can be dielectric rods in the air, i.e., rod slab, or air holes in a dielectric material, i.e., hole slab. The band diagrams of an example square lattice rod slab with a rod diameter of $0.4a$ and thickness of $2a$ and hexagonal lattice hole slab with a hole diameter of $0.6a$ and thickness of $0.5a$ are given in Figure 2.5a and 2.5b, respectively.

The modes propagating in air constitute light cones, colored in gray in Figure 2.5. The modes lying below the light cones are confined in the slab and attenuate exponen-

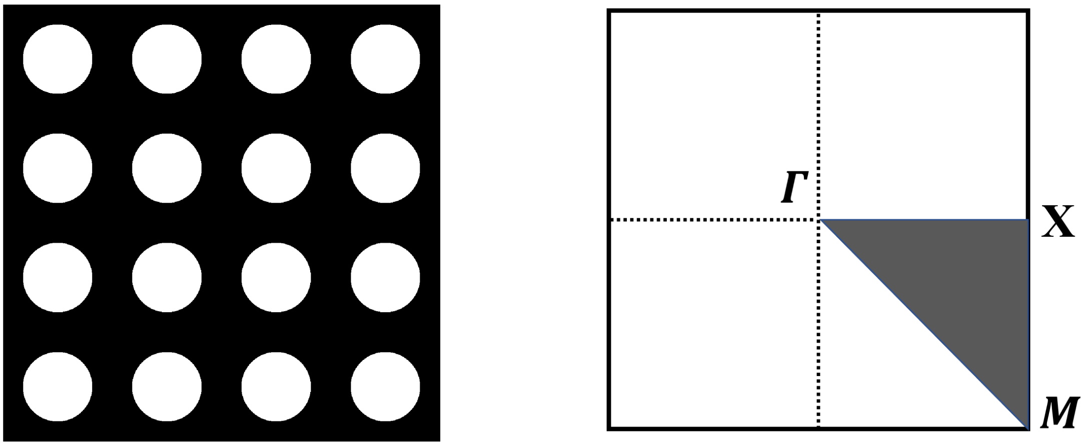

(a) Square lattice in the spatial domain, i.e., real lattice.

(b) Brillouin zone of square lattice in momentum space, i.e., reciprocal lattice.

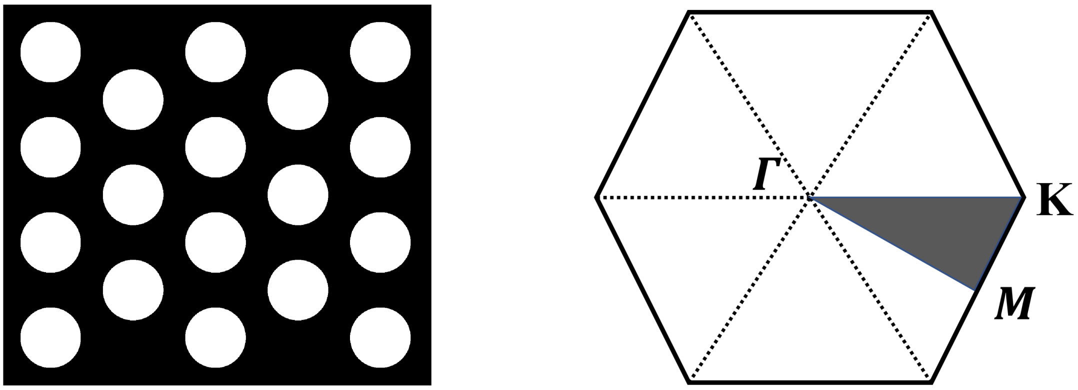

(c) Hexagonal lattice in the spatial domain, i.e., real lattice.

(d) Brillouin zone of hexagonal lattice in momentum space, i.e., reciprocal lattice.

Figure 2.4: The irreducible Brillouin zone for 2D photonic crystals.

tially away from the slab. It is worth noting that rod slabs have a complete bandgap for transverse magnetic (TM) fields, while hole slabs have a complete bandgap for transverse electric (TE) fields.

The band structures given in Figure 2.5 were obtained using MIT Photonic Bands (MPB) [25] software. MPB is non-commercial software that can analyze waveguides and modulators containing periodic dielectric structures, such as photonic crystals, to compute band structures and electromagnetic modes via global plane wave expansion. It was used in the optical modulator design, described in Chapter 3.

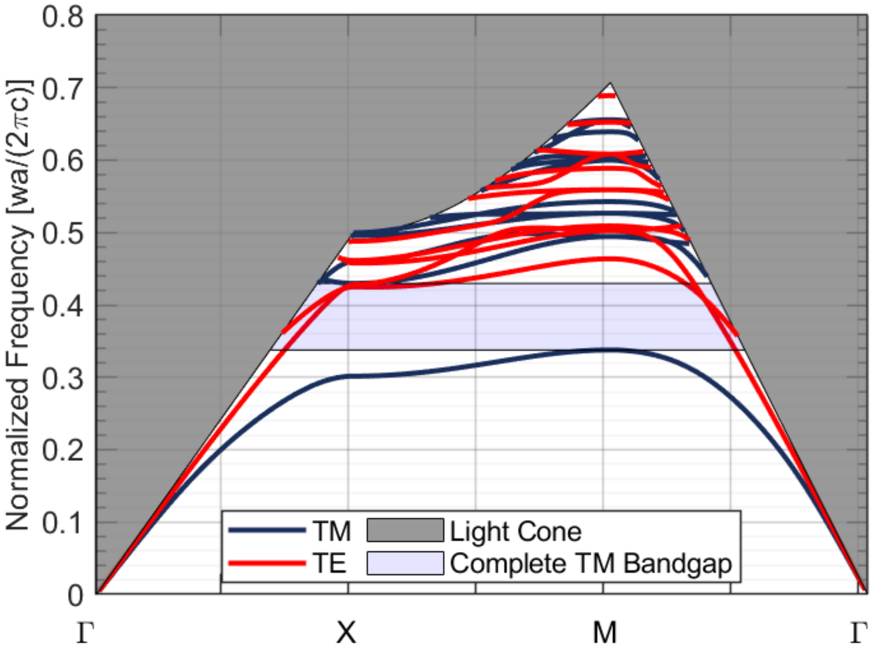

(a) For dielectric rods in air.

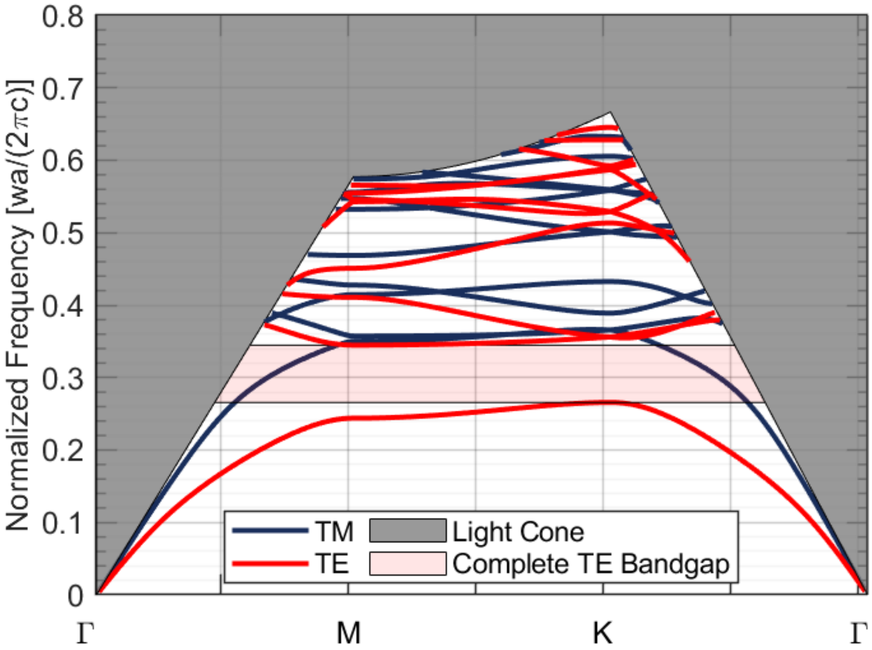

(b) For air holes in a dielectric material.

Figure 2.5: Band diagrams of photonic crystal slabs. Calculated via MPB.

2.4 Band-to-Band Transition Mechanism

The refractive index is a fundamental optical parameter helpful in explaining the phenomena such as reflection, refraction, and light propagation in a medium with dielectric constant $\epsilon(\vec{r})$. It is defined as the ratio between the speed of light in free space (c) and in a dielectric medium (v), as described in Equation 2.26.

$$\frac{c}{n} = v = \lambda * f = \frac{w}{k} \tag{2.26}$$

Here, λ and f represent the wavelength and the frequency of the light in a dielectric medium.

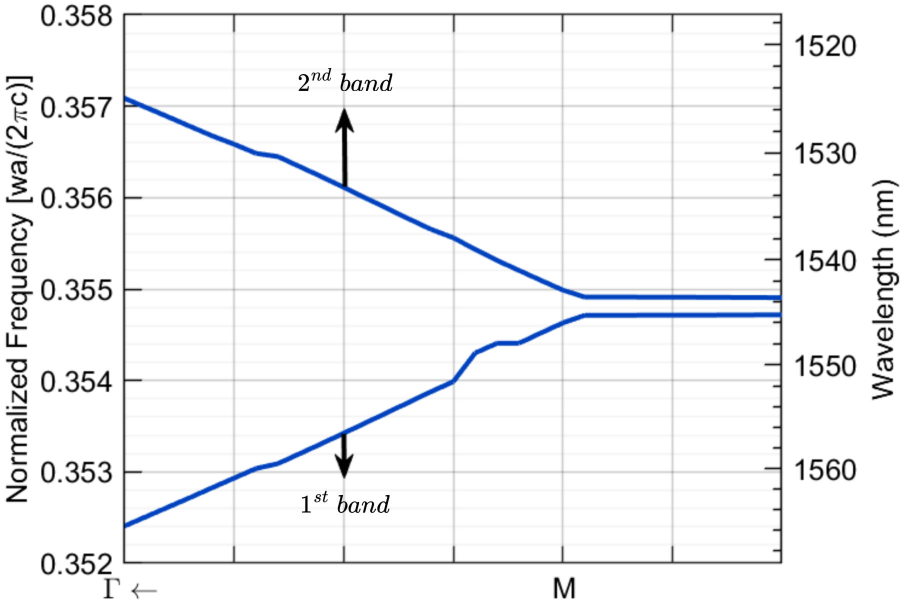

Figure 2.6: TM bands for hexagonal lattice photonic crystals at the direction of Γ - M.

In the case of photonic crystals, the refractive index is different than that of bulk materials. The TM bands for hexagonal lattice photonic crystals with a period of 550 nm, hole diameter of 350 nm, and silicon refractive index of 3.48 at the direction of Γ - M are given in Figure 2.6. For these two bands, the effective refractive index can be expressed as:

$$n_{eff}(w) = \begin{cases} \frac{+k*c}{w}, & for\ 1^{st}\ band \\ \frac{-k*c}{w}, & for\ 2^{nd}\ band \end{cases} \tag{2.27}$$

Here, the second line in Equation 2.27 illustrates negative refraction phenomena.

If photons can move between the first and second bands, the corresponding effective refractive index difference would be $|\Delta n_{eff}| = 2\frac{k*c}{w}$. This large refractive index difference could be beneficial in decreasing the length of a phase shifter, which will be further investigated in Chapter 3.

CHAPTER 3

MODULATOR DESIGN

In this chapter, an MZI photonic crystal modulator design based on band-to-band transition proposed in [13, 26] is investigated, and further improvements are explored.

3.1 Overview of Modulator Operation

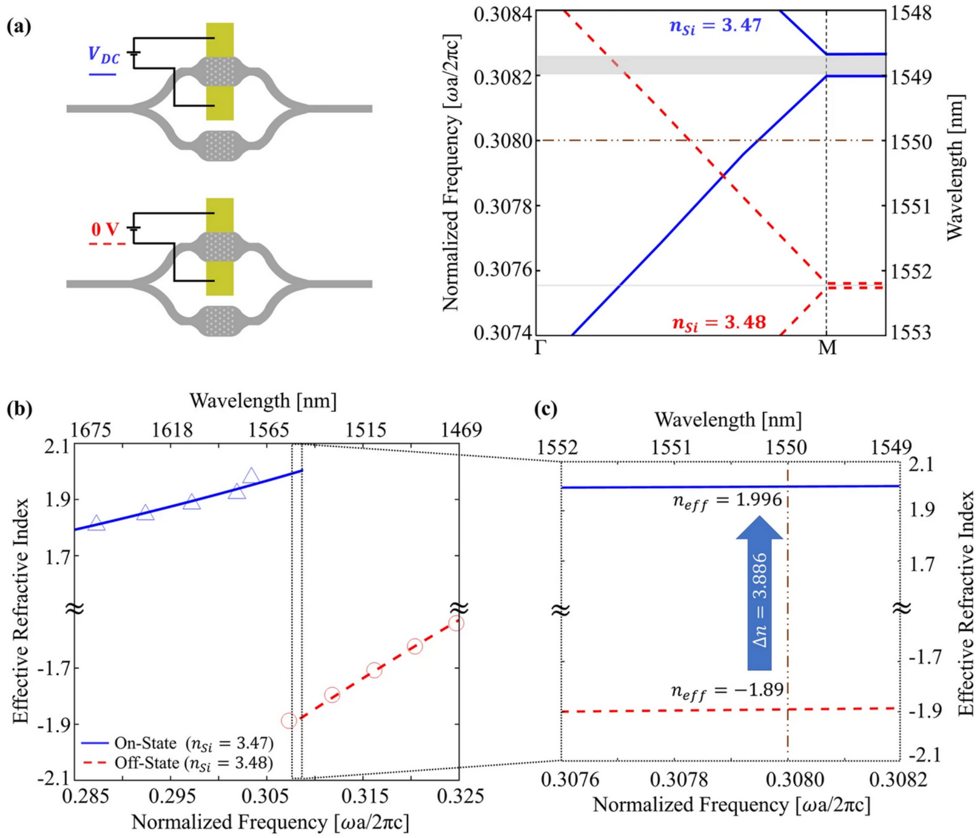

Figure 3.1: Summary of the operation mechanism of the modulator design [13].

The operation of the previously proposed modulator is briefly illustrated in Figure 3.1. When a sufficiently large bias voltage is applied to the active region of MZI at one of its arms, the refractive index of the silicon is changed due to the plasma dispersion effect.

The small change in the refractive index of silicon creates a shift in the bands. If the operating wavelength is appropriately selected, the photons would be transferred between the 1^{st} and 2^{nd} bands, corresponding to the transfer between the positive and negative effective refractive indexes. Such a transfer can achieve a significantly large effective index change.

This previous design was based on a silicon-on-insulator (SOI) wafer with 286 nm silicon thickness; however, our group use SOI wafers with 260 nm silicon thickness. Moreover, the previous experimental works on the proposed design demonstrated all-optical modulation but failed at modulation with PIN diodes [27]. For these reasons, the design of the modulator was reexamined, as described in this chapter.

3.2 Design of Photonic Crystal Region

3.2.1 Bandgap Optimization

The modulator operation requires a narrow bandgap between the 1^{st} and 2^{nd} TM bands to allow band-to-band transition under small silicon refractive index changes. This TM bandgap should be between 1500-1630 nm to be suitable for the emission range of lasers in our laboratory. More details of the experimental setup are given in Chapter 4.2. Lastly, it is aimed to have a large TE bandgap at operation wavelengths to inherently pass only TM light. To optimize the photonic bandgap's location and width, MPB software was used, and the band structures of the photonic crystal slabs with hexagonal lattice on the SOI wafer with 260 nm silicon layer for varying periods and hole diameters were obtained.

The TE and TM band structures of the photonic crystal with hexagonal lattice with hole diameters of 350 nm and period of 550 nm are given in Figure 3.2.

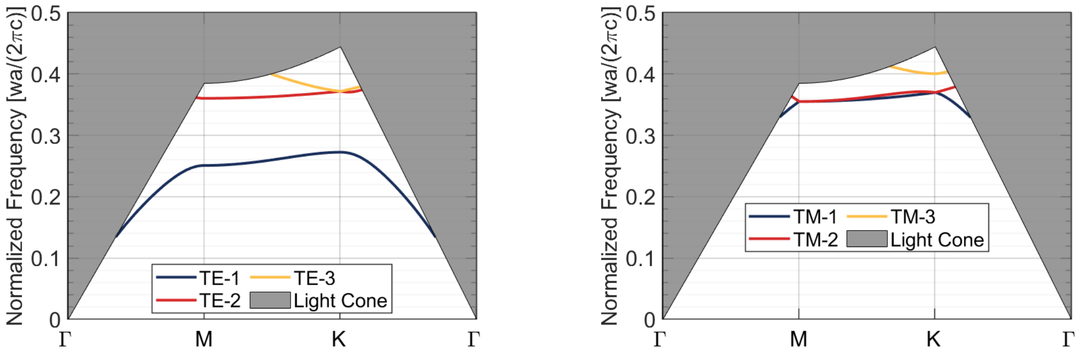

(a) TE bands.

(b) TM bands.

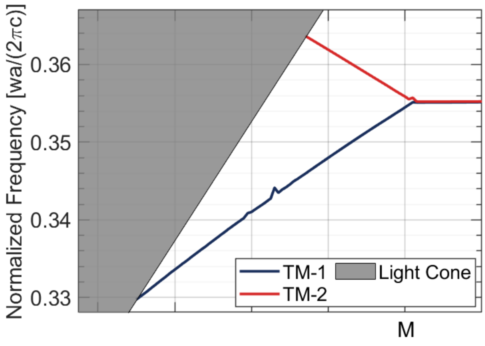

(c) TM bands zoomed in Γ - M direction.

Figure 3.2: Band diagram for hexagonal lattice photonic crystals with hole diameters of 350 nm and period of 550 nm.

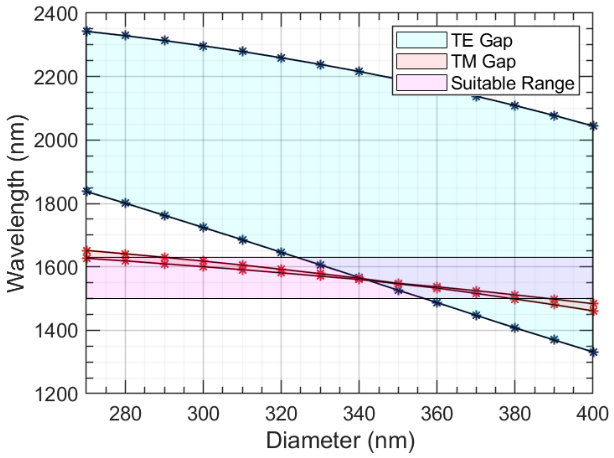

Figure 3.3: TE $\&$ TM gaps for $a = 550\ nm$ at Γ - M direction.

The information presented in band structures such as Figure 3.2 can be extracted to determine the spectrum's TE and TM bandgap regions. Figure 3.3 illustrates the TE and TM bandgaps for varying hole diameters from 270 nm to 400 nm for photonic crystals with a period of 550 nm at the direction of Γ - M. The TE and TM gap regions and regions in which our experimental setup is suitable for modulation experiments are colored cyan, red and purple, respectively, for the rest of the figures in this subsection.

The TE and TM bandgaps for varying hole diameters from 305 nm to 375 nm for photonic crystals with periods of 540, 550, and 560 nm at the direction of Γ - M are depicted in Figure 3.4. It is seen that photonic crystals with a 550 nm period and 350 nm hole diameter have a minimal TM gap at 1550 nm, which happens to overlap with the TE gap. Therefore, the crystal period and the hole diameter for photonic crystals in the direction of Γ - M were selected as 550 nm and 350 nm, respectively.

The analysis performed for hexagonal photonic crystal hole slabs with light propagating in the Γ - M direction is repeated for the light propagating in the Γ - K direction. The TE and TM band structures of photonic crystal with hexagonal lattice with hole diameters of 280 nm and period of 550 nm are given in Figure 3.5.

The TE and TM bandgaps for photonic crystal with a period of 550 nm at the direction of Γ - K for varying hole diameters from 170 nm to 350 nm are depicted in Figure 3.6. It is seen that the width of the TM gap is close to zero for variations of period and crystal diameter.

The hexagonal lattice using the same circular hole sizes possesses a C_{6V} symmetry group[28, 29]. Here, C_{6V} represents the cyclic symmetry of angle $\pi/6$ around the rotation axis with additional 6 mirror planes containing the rotation axis [30]. Due to C_{6V} symmetry of the hexagonal lattice, there exists a Dirac point (cone) at the K point (for photonic crystals with time-reversal symmetry) [29, 31, 32]. The first and second TM bands are in contact at K point [31].

The TE and TM bandgaps for varying hole diameters from 245 nm to 305 nm for photonic crystals with periods of 540, 550, and 560 nm in the direction of Γ - K are depicted in Figure 3.7. Neither of them has an overlap between the TM and TE gaps.

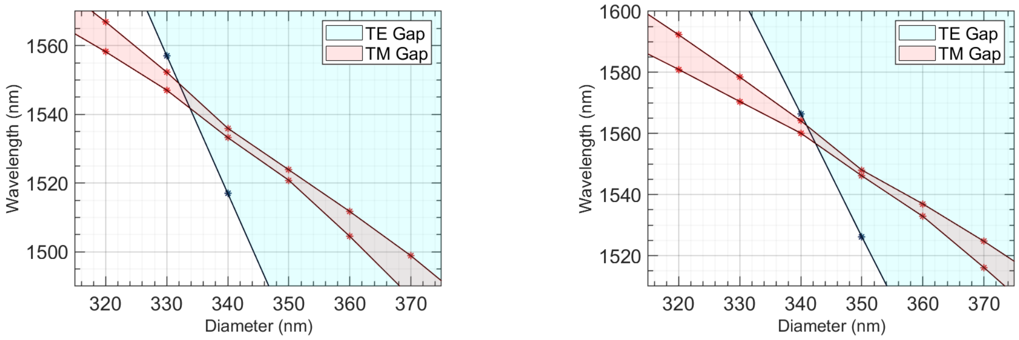

(a) $a = 540\ nm$.

(b) $a = 550\ nm$.

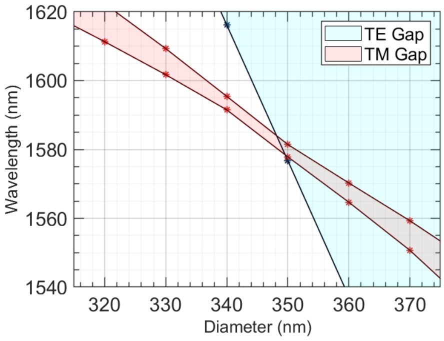

(c) $a = 560\ nm$.

Figure 3.4: TE & TM gaps, for photonic crystals at Γ - M direction.

Actually, the overlap around 1550 nm can be achieved for periods larger than 620 nm. However, the period of the photonic crystal was selected as 550 nm for the easiness in the fabrication, and the hole diameter was chosen as 280 nm for photonic crystals in the direction of Γ - K.

3.2.2 Phase Difference Calculations

Another condition for successful modulation operation is to achieve destructive interference when the band-to-band transition happens. This requires careful selection of the number of crystals in the propagation direction. Here, the phase difference created by photonic crystal regions with a triangular lattice is examined.

The dispersion curve for a photonic crystal slab along an arbitrary crystal direction is

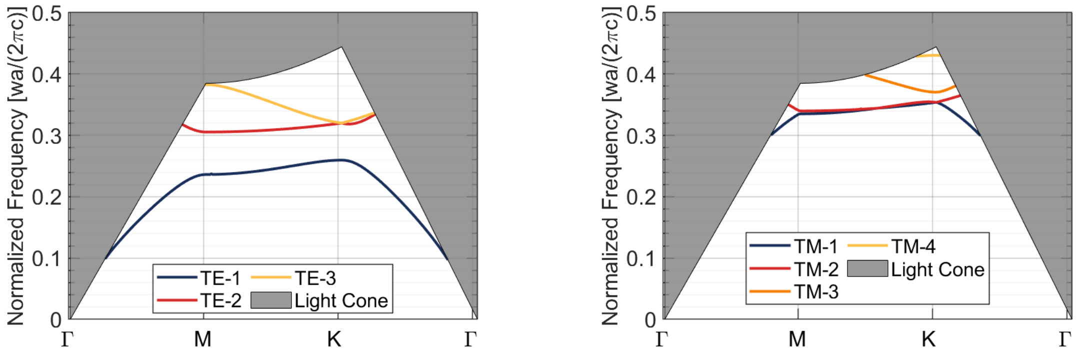

(a) TE bands.

(b) TM bands.

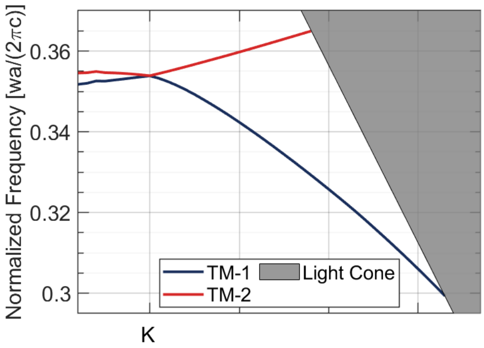

(c) TM bands, zoomed in Γ - K direction.

Figure 3.5: Band diagram for hexagonal lattice photonic crystals with hole diameters of 280 nm and period of 550 nm.

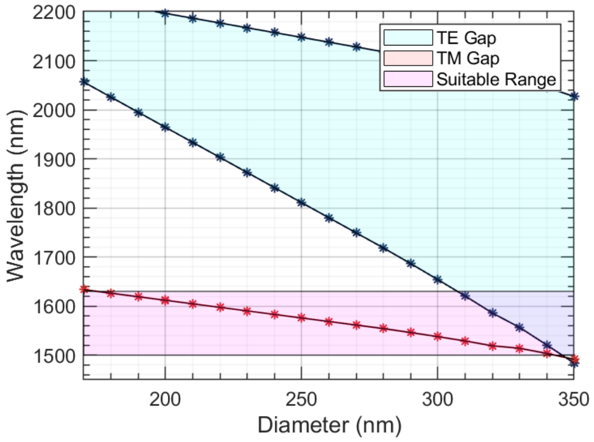

Figure 3.6: TE $\&$ TM gaps for $a = 550\ nm$ at Γ - K direction.

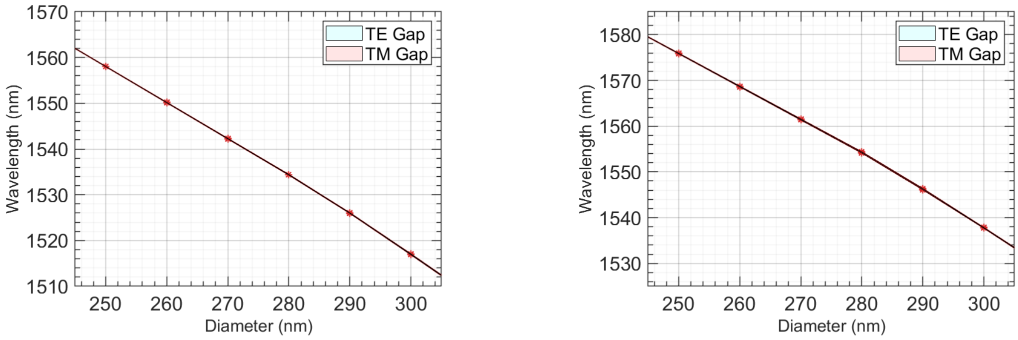

(a) $a = 540\ nm$.

(b) $a = 550\ nm$.

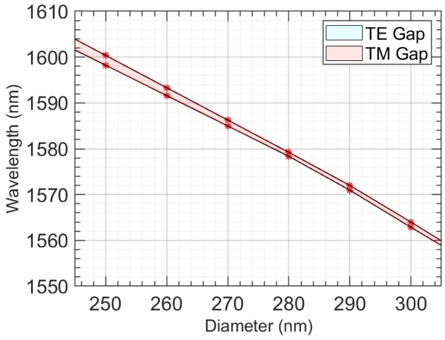

(c) $a = 560\ nm$.

Figure 3.7: TE & TM gaps, for photonic crystals at Γ - K direction.

depicted in Figure 3.8.

Defining N as the average number of photonic crystals in the horizontal direction for MZIs, w_{mid} as the frequency at the intersection point seen in Figure 3.8, and w_{op} as the operation frequency (in rad); and starting by expressing optical path difference (OPD) as the function of photonic crystal length (L), we can write the following equations:

$$OPD = \Delta\left(L * n\right)\big|_{PhC} = L * \Delta n = (N - 0.5) * \sqrt{3} * a * \Delta n \tag{3.1}$$

The condition for constructive and destructive interference can be written as follows:

$$\begin{aligned} \frac{mod\left(OPD,\ \lambda\right)}{\lambda} &= \frac{mod\left((N-0.5) * \sqrt{3} * a * \Delta n, \lambda\right)}{\lambda} \\ &= \begin{cases} 0, & perfect\ constructive\ interference \\ 0.5, & perfect\ destructive\ interference \end{cases} \end{aligned} \tag{3.2}$$

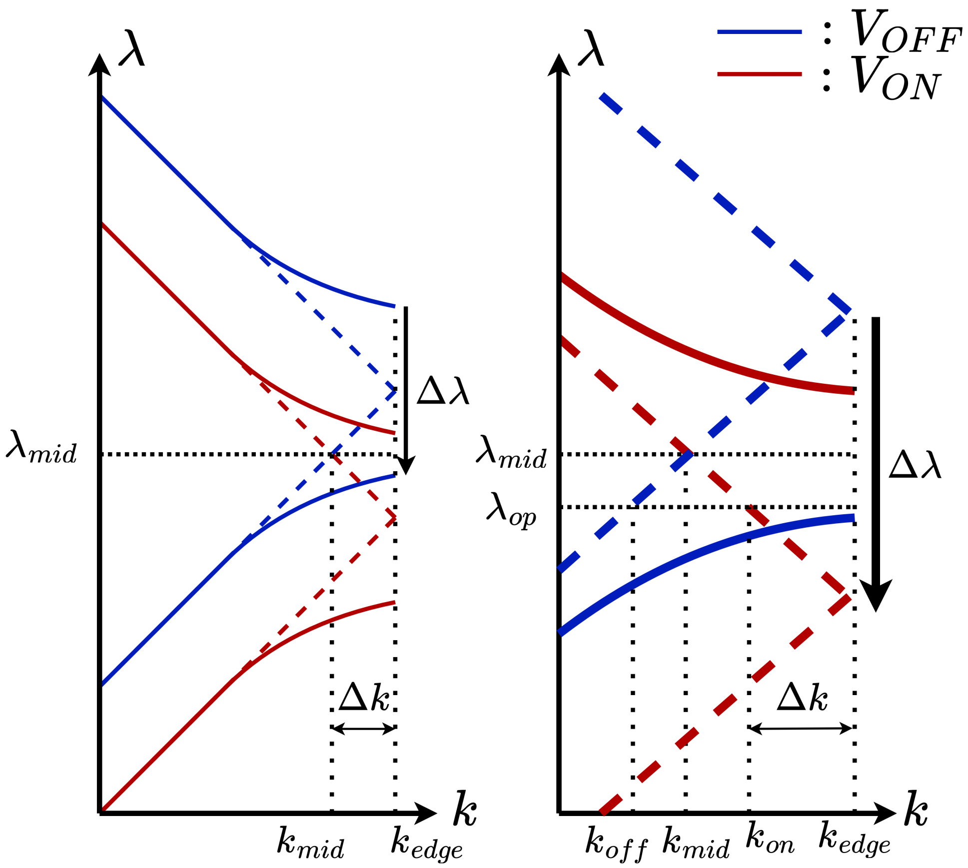

Figure 3.8: An arbitrary wavelength vs. wave vector graph for V_{ON} and V_{OFF}.

The wavelength (λ) and $\frac{OPD}{\lambda}$ can be expressed as the function of frequency (w) as:

$$\lambda = \frac{2 * \pi * c}{w} \tag{3.3}$$

$$\frac{OPD\,(w)}{\frac{2*\pi*c}{w}} = \frac{(N - 0.5) * \sqrt{3} * a * \Delta n}{\frac{2*\pi*c}{w}} \tag{3.4}$$

Using Equation 2.27, the effective refractive index change can be written as:

$$\Delta n_{eff}\,(w_{op}) = n_{eff}\,(V_{ON}) - n_{eff}\,(V_{OFF}) = \frac{k_{on} * c}{w_{op}} + \frac{k_{off} * c}{w_{op}} \tag{3.5}$$

Assuming $k_{on} \cong k_{off}$ at operation wavelength, we can further write the following equations:

$$|k_{mid}| \cong \frac{|k_{on}| + |k_{off}|}{2} \tag{3.6}$$

$$\Delta n_{eff}\,(w_{op}) \cong \frac{|k_{mid}| * c}{w_{op}} * 2 \tag{3.7}$$

$$\frac{OPD\,(w_{op})}{\frac{2*\pi*c}{w_{op}}} = \frac{(N - 0.5) * \sqrt{3} * a * (\frac{|k_{mid}|*c}{w_{op}} * 2)}{\frac{2*\pi*c}{w_{op}}} \tag{3.8}$$

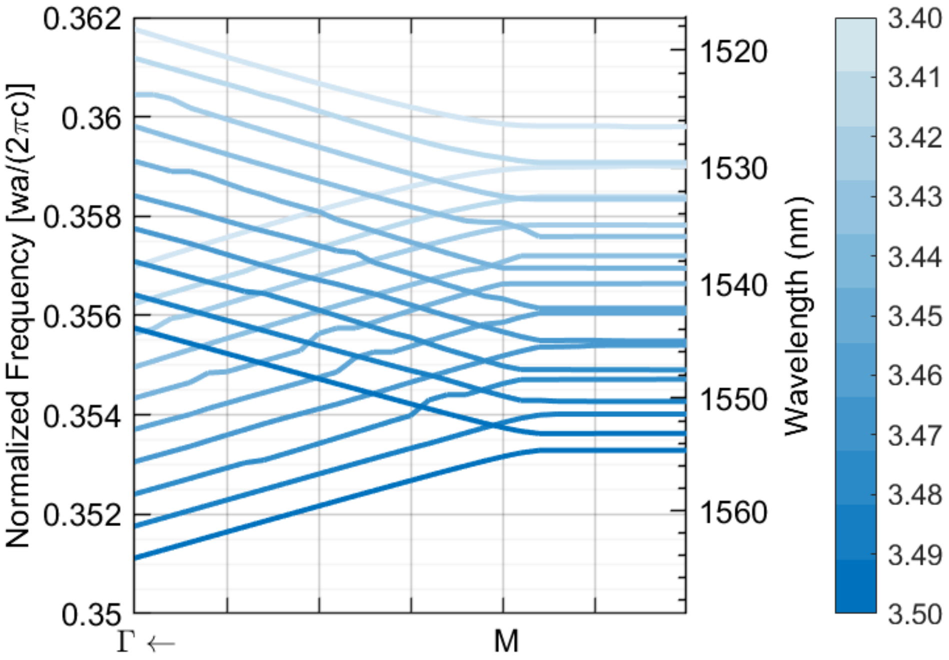

Figure 3.9: The shift of TM bands for hexagonal lattice photonic crystals with a period of 550 nm and hole diameter of 350 nm at the direction of Γ - K for varying silicon refractive index.

Information on the amount of shift at bands can be extracted from the band structure given in Figure 3.9). From there, $|k_{mid}\,(\Delta n)|$ can be calculated:

$$\Delta\ \lambda|_{\lambda\cong 1550\ nm,\ \Delta n_{Si}=0.01} \cong 3\ nm \tag{3.9}$$

$$\Delta\lambda\,(\Delta n) \cong 3nm * \frac{\Delta n}{0.01} \tag{3.10}$$

$$\frac{\Delta k\,(\Delta n)}{|k_{edge}|} = \frac{\Delta\lambda\,(\Delta n)}{1550nm} = \frac{3nm}{1550nm} * \frac{\Delta n}{0.01} \cong \frac{\Delta n}{5.166} \tag{3.11}$$

$$|k_{mid}\,(\Delta n)| = |k_{edge}| - \Delta k\,(\Delta n) = |k_{edge}| * \left[1 - \frac{\Delta n}{5.166}\right] \tag{3.12}$$

Finally, we reached the final equation for general phase difference calculations around 1550 nm:

$$\frac{OPD}{\lambda} = (N - 0.5) * \sqrt{3} * 2 * \left[\frac{(|k_{edge}| * a)}{2 * \pi}\right] * \left[1 - \frac{\Delta n}{5.166}\right] \tag{3.13}$$

From Figure 3.10, we can write the following expressions:

$$k_M = 0.5\,G_1,\ |k_M| * \frac{a}{2 * \pi} = \frac{1}{\sqrt{3}} \cong 0.577 \tag{3.14}$$

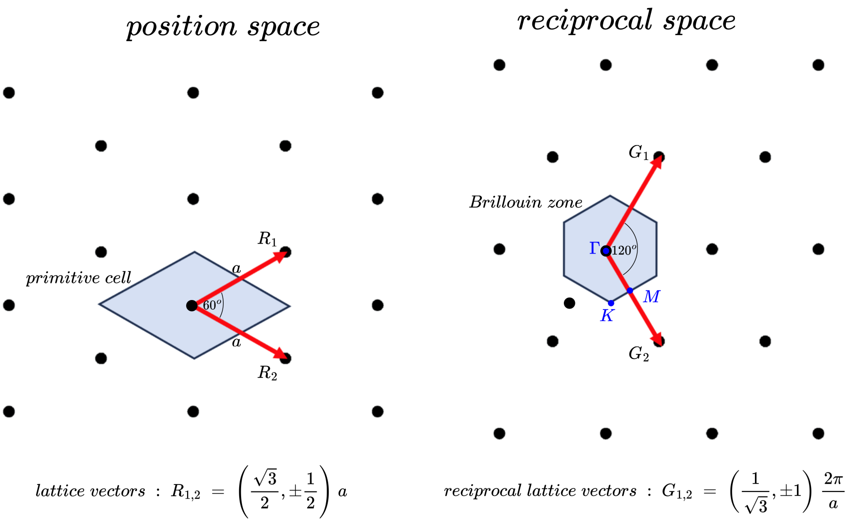

Figure 3.10: The lattice diagram for position and reciprocal spaces. Redrawn after [22].

$$k_K = \frac{1}{3}G_1 + \frac{1}{3}G_2,\ |k_K| * \frac{a}{2 * \pi} = \frac{2}{3} \cong 0.666 \tag{3.15}$$

In the case of Γ - M, $k_{edge} = k_M$ and $\frac{OPD}{\lambda}$ is given as:

$$\begin{aligned} \left.\frac{OPD}{\lambda}\right|_M &= (N - 0.5) * \sqrt{3} * 2 * \frac{1}{\sqrt{3}} * \left[1 - \frac{\Delta n}{5.166}\right] \\ &= (N - 0.5) * 2 * \left[1 - \frac{\Delta n}{5.166}\right] \end{aligned} \tag{3.16}$$

According to Equation 3.16, $\frac{OPD}{\lambda}\big|_M$ is close to integer values for small N numbers. Therefore, it is not possible to achieve destructive interference at relatively small N numbers. For the solution, Γ -K direction can be used, where $k_{edge} = k_K$. In this case, $\frac{OPD}{\lambda}$ becomes:

$$\begin{aligned} \left.\frac{OPD}{\lambda}\right|_K &= (N - 0.5) * \sqrt{3} * 2 * \frac{2}{3} * \left[1 - \frac{\Delta n}{5.166}\right] \\ &\cong (N - 0.5) * 2.3094 * \left[1 - \frac{\Delta n}{5.166}\right] \end{aligned} \tag{3.17}$$

The evaluated $\frac{OPD}{\lambda}$ based on MPB data via Equation 3.2 and based on derived Equation 3.16 are tabulated in Table 3.1 and Table 3.2, respectively. Comparing the tables, we can conclude that the derived Equation 3.16 is equivalent to Equation 3.2.

The evaluated $\frac{OPD}{\lambda}$ based on the derived Equation 3.17 are tabulated in Table 3.3.

Table 3.1: The optical path difference/wavelength calculated using Equation 3.2, for $a = 550\ nm$ and $D = 350\ nm$.

$n_{Si,on}$		3.47	3.46	3.45	3.44	3.43	
Δn_{Si}		0.01	0.02	0.03	0.04	0.05	
a		550	550	550	550	550	
$\Delta n_{eff.avg}$		3.251	3.241	3.233	3.223	3.212	
λ_{avg}		1551.4	1550.8	1549.9	1548	1546	
N	6.0	10.978	10.950	10.928	10.907	10.886	OPD/λ
	7.0	12.974	12.941	12.915	12.890	12.865	
	8.0	14.971	14.932	14.902	14.873	14.844	
	9.0	16.967	16.923	16.889	16.856	16.823	
	10.0	18.963	18.913	18.876	18.839	18.802	
	11.0	20.959	20.904	20.863	20.823	20.782	
	12.0	22.955	22.895	22.850	22.806	22.761	
	13.0	24.951	24.886	24.837	24.789	24.740	
	14.0	26.947	26.877	26.824	26.772	26.719	
	15.0	28.943	28.868	28.811	28.755	28.698	
	16.0	30.939	30.859	30.798	30.738	30.678	
	17.0	32.935	32.850	32.785	32.721	32.657	
	18.0	34.931	34.841	34.771	34.704	34.636	

Table 3.2: The optical path difference/wavelength calculated using Equation 3.16.

$n_{Si,on}$		3.47	3.46	3.45	3.44	3.43	
Δn_{Si}		0.01	0.02	0.03	0.04	0.05	
N	6.0	10.979	10.957	10.936	10.915	10.894	OPD/λ
	7.0	12.975	12.950	12.925	12.899	12.874	
	8.0	14.971	14.942	14.913	14.884	14.855	
	9.0	16.967	16.934	16.901	16.868	16.835	
	10.0	18.963	18.926	18.890	18.853	18.816	
	11.0	20.959	20.919	20.878	20.837	20.797	
	12.0	22.955	22.911	22.866	22.822	22.777	
	13.0	24.952	24.903	24.855	24.806	24.758	
	14.0	26.948	26.895	26.843	26.791	26.739	
	15.0	28.944	28.888	28.832	28.775	28.719	
	16.0	30.940	30.880	30.820	30.760	30.700	
	17.0	32.936	32.872	32.808	32.744	32.681	
	18.0	34.932	34.864	34.797	34.729	34.661	

Table 3.3: The optical path difference/wavelength calculated using Equation 3.17.

$n_{Si,on}$		3.47	3.46	3.45	3.44	3.43	
Δn_{Si}		0.01	0.02	0.03	0.04	0.05	
N	6	12.677	12.653	12.628	12.603	12.579	OPD/λ
	6.5	13.830	13.803	13.776	13.749	13.722	
	7	14.982	14.953	14.924	14.895	14.866	
	7.5	16.135	16.103	16.072	16.041	16.009	
	8	17.287	17.253	17.220	17.186	17.153	
	8.5	18.439	18.404	18.368	18.332	18.296	
	9	19.592	19.554	19.516	19.478	19.440	
	9.5	20.744	20.704	20.664	20.624	20.583	
	10	21.897	21.854	21.812	21.769	21.727	
	10.5	23.049	23.005	22.960	22.915	22.870	
	11	24.202	24.155	24.108	24.061	24.014	
	11.5	25.354	25.305	25.256	25.207	25.158	
	12	26.507	26.455	26.404	26.352	26.301	

Considering the results, the number of crystals in the propagation direction was selected as $N = 8.5$, corresponding to a phase shifter length of 4.4 μm.

3.3 Design of PIN Diode

The PIN diode is designed to provide sufficient electron and hole concentration. The carrier's behavior in the active region of the MZI was investigated via a commercial semiconductor simulation software, Sentaurus TCAD [33]. The cross-section of the MZI active region and PIN diode is given in Figure 3.11.

Based on the experimental doping characteristics (40 nanometers of junction depth and peak concentration of $5 \times 10^{18}\ cm^{-3}$), the concentration of boron and phosphorus doped regions for varying silicon depth is estimated as in Figure 3.12. This shallow doping profile was sufficient to deplete and inject the carriers inside the optically active region, allowing the desired refractive index to change [15].

The carrier concentrations under no bias voltage, and electron concentration and hole concentration, when a current of 85 μA is injected, are provided in Figures 3.13-3.15,

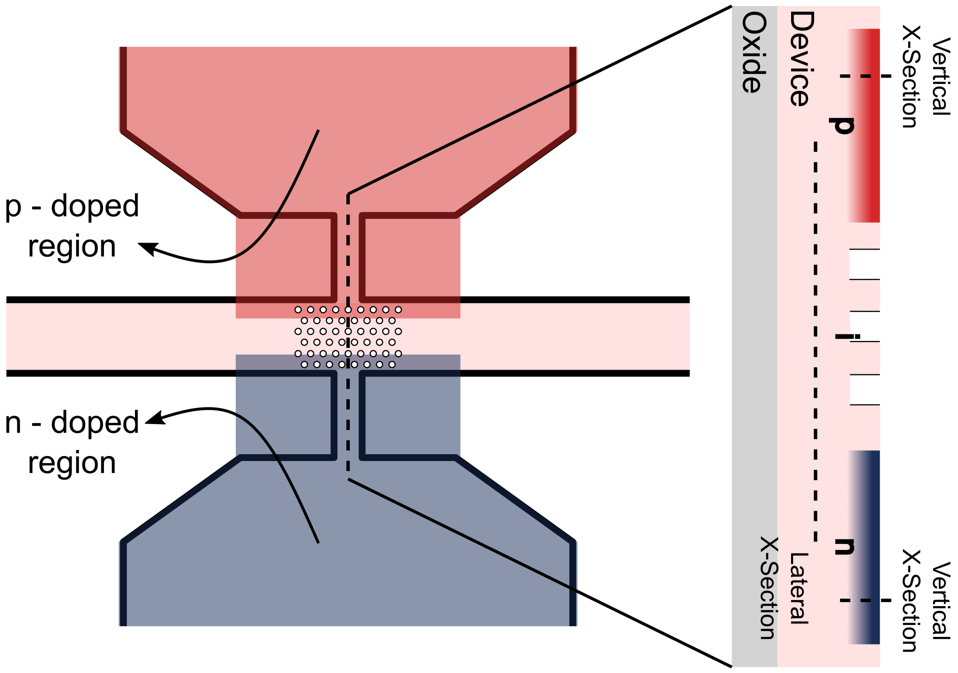

Figure 3.11: PIN diode, MZI active region, and their cross-section.

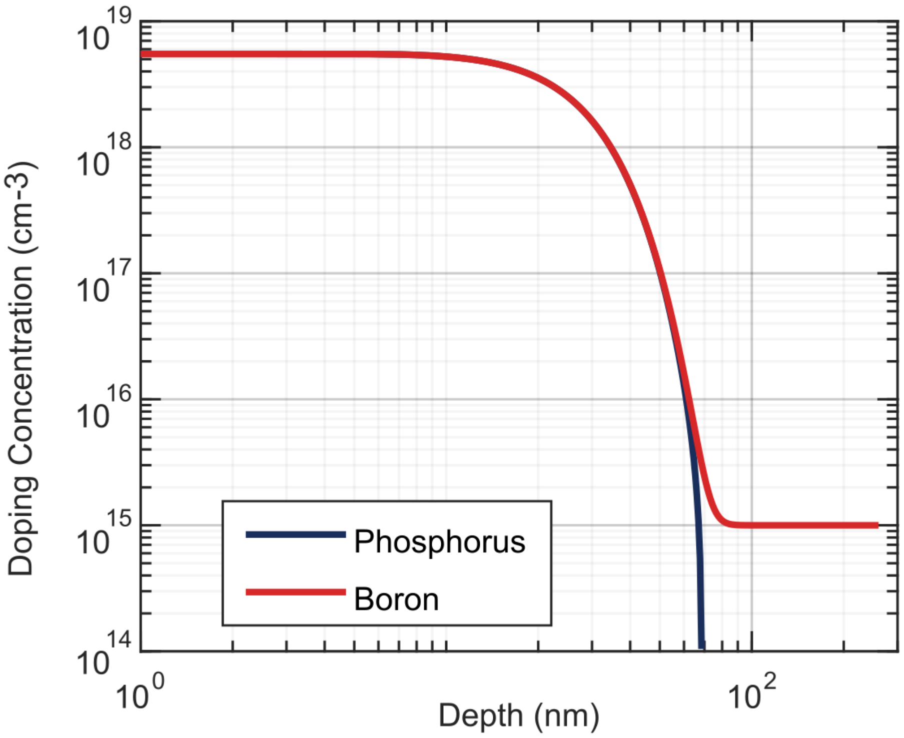

Figure 3.12: Doping concentration for varying silicon depths.

respectively.

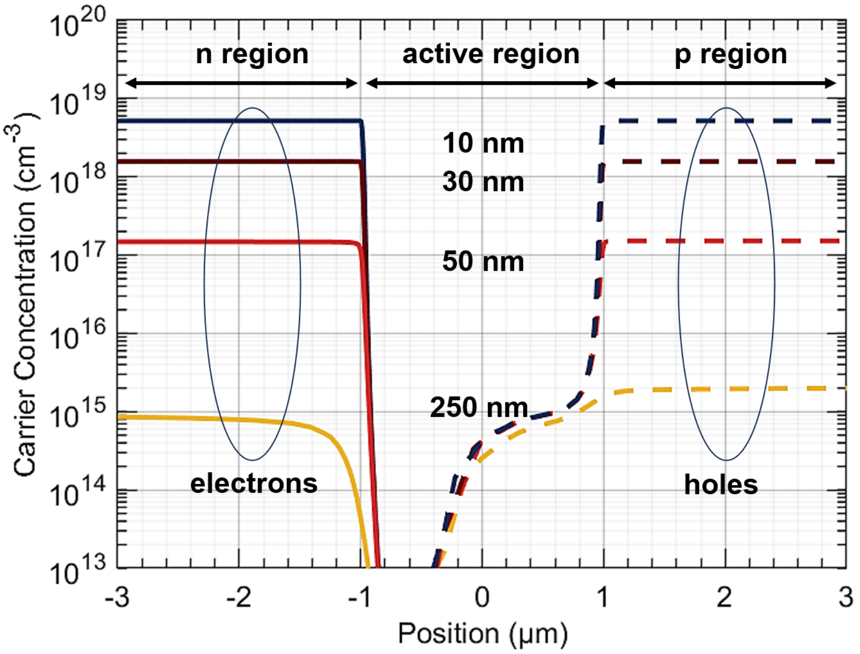

Figure 3.13: Carrier concentrations under no bias voltage in the active region for silicon depth varying from 10 nm to 250 nm.

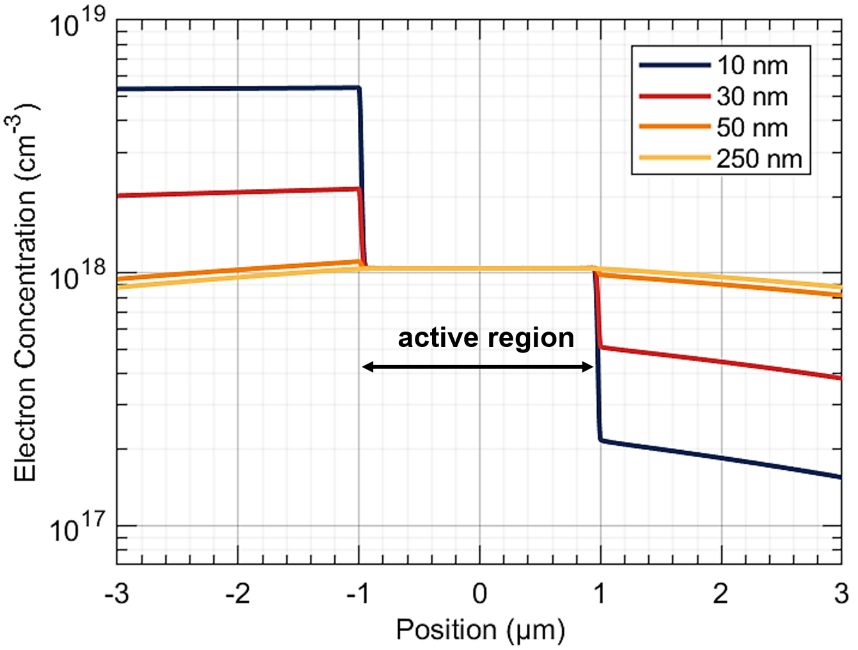

Figure 3.14: Electron concentration under bias voltage in the active region for silicon depth varying from 10 nm to 250 nm when 85 μA current passes through the diode.

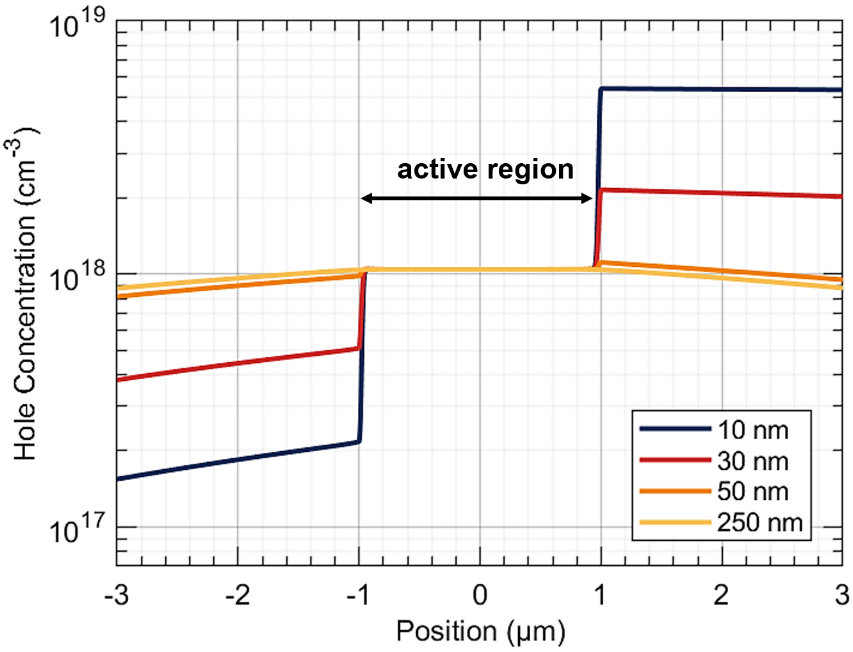

Figure 3.15: Hole concentration under bias voltage in the active region for silicon depth varying from 10 nm to 250 nm when 85 μA current passes through the diode.

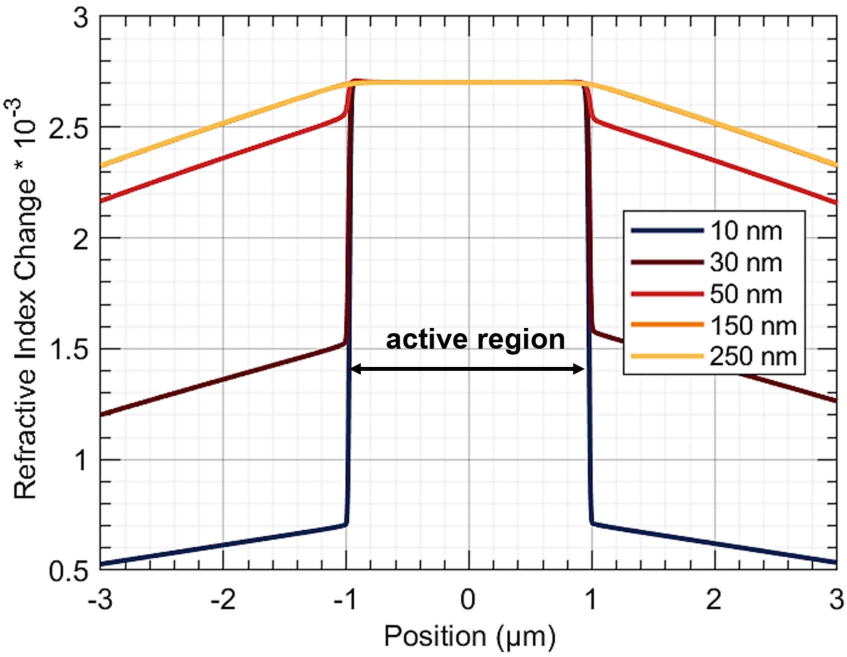

Figure 3.16: Change of refractive index of silicon in the active region for silicon depth varying from 10 nm to 250 nm when 85 μA current passes through the diode.

When carrier concentration along the junction is investigated, carrier densities on the order of $10^{15}\ cm^{-3}$ can be observed, as shown in Figure 3.13. This is the unintentional doping density of the SOI wafer. The number of carriers can be increased to the order of $10^{18}\ cm^{-3}$, as shown in Figure 3.14 and Figure 3.15, when a current of 85 μA is injected at 290 K. Moreover, carriers were distributed inside the active region homogeneously, independent of the depth.

Based on the results given in Figures 3.13-3.15, the evaluation of Equation 1.8 leads to a refractive index change of $2.7 * 10^{-3}$ in the active region, as illustrated in Figure 3.16.

CHAPTER 4

RESULTS AND DISCUSSIONS

4.1 Fabrication and SEM Imaging

The fabrication of the waveguides and MZIs with photonic crystal regions, as described in Chapter 3, was completed in two steps. In the first step, the etching of the silicon layer of the SOI wafer was performed at Sabancı University by Dr. Cenk Yanık using reactive ion etching (RIE). At this step, structures such as ridge waveguides, MZIs, and air holes that constitute photonic crystals were created. In the second step, the chip was processed in Quantum Devices and Nanophotonics Research Laboratory (KANAL) at METU by Alper Şahin to form lateral PIN diodes on the arms of the MZIs. P and N doping and metal (M) layers were deposited during this process.

Our previous experiences showed us that the diameters of the air holes etched on the silicon tend to enlarge by 30-60 nm. Considering this, we fabricated waveguides and MZIs with varying photonic crystal dimensions. Later, the dimensions of the fabricated photonic crystals were measured using a scanning electron microscope (SEM).

SEM is a method to image nanostructures and is used to check the quality of the fabrication process. Example SEM images of the fabricated ridge waveguides with photonic crystal regions in the Γ - M and Γ - K directions, MZI active region with photonic crystals in the Γ - M and Γ - K directions with each side covered with photonic crystals in the Γ - M direction are given in Figures 4.1-4.4, respectively.

In this section, the results obtained on our two latest samples (labeled as Sample 1 and Sample 2) were examined. Based on the measurements on SEM images of Sample 1,

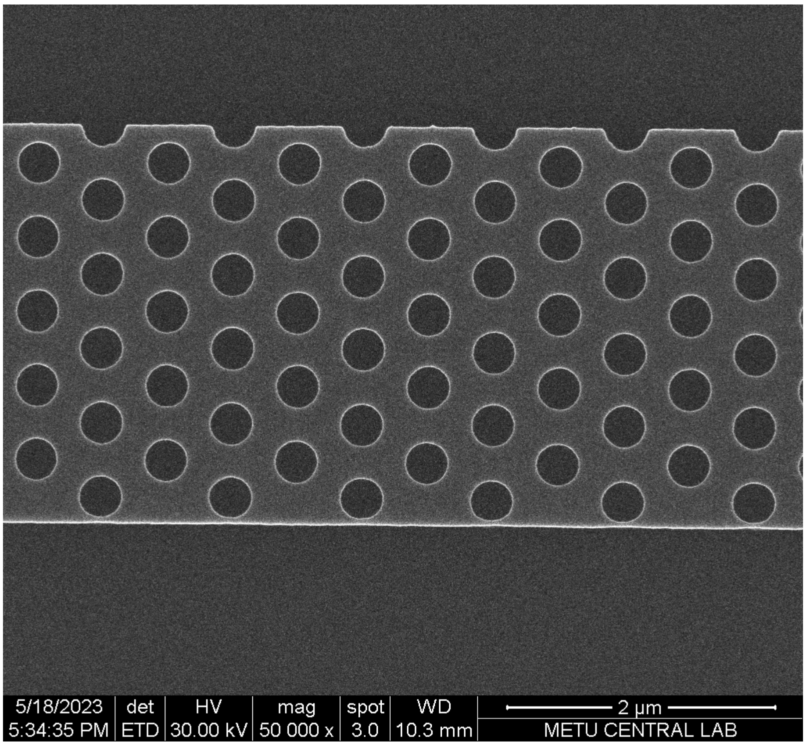

Figure 4.1: Waveguide with PhCs at Γ - M direction.

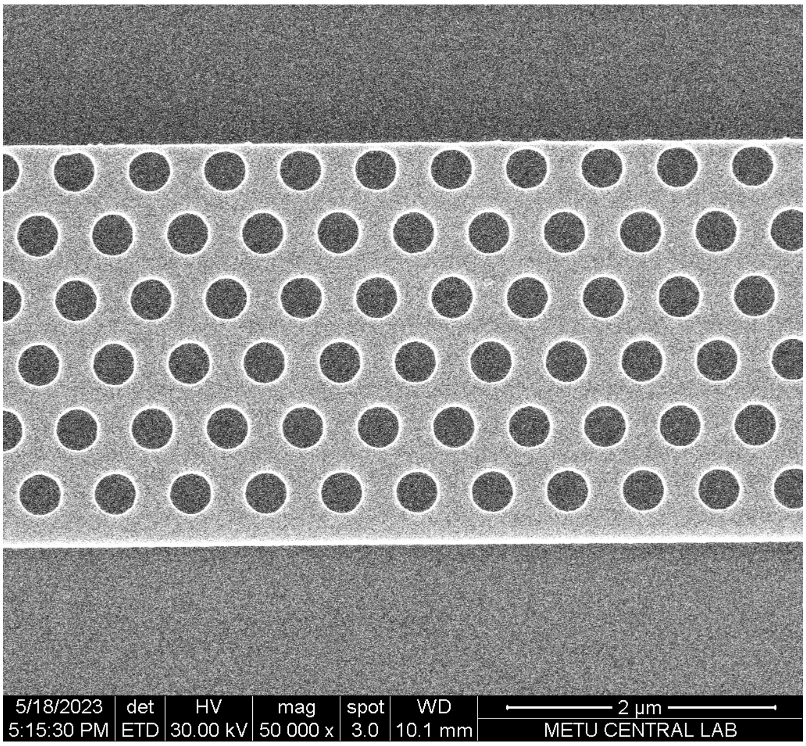

Figure 4.2: Waveguide with PhCs at Γ - K direction.

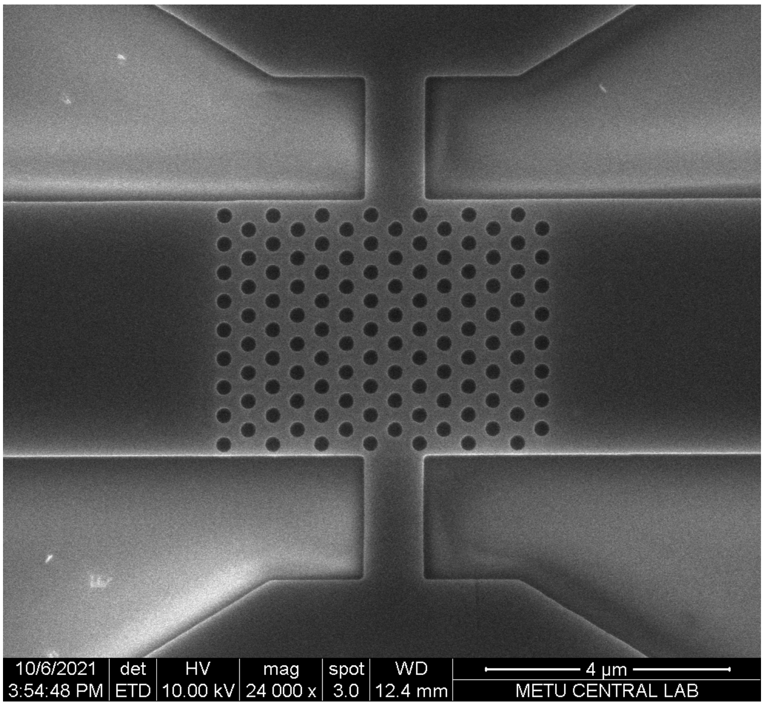

Figure 4.3: MZI active region with PhCs at Γ - M direction.

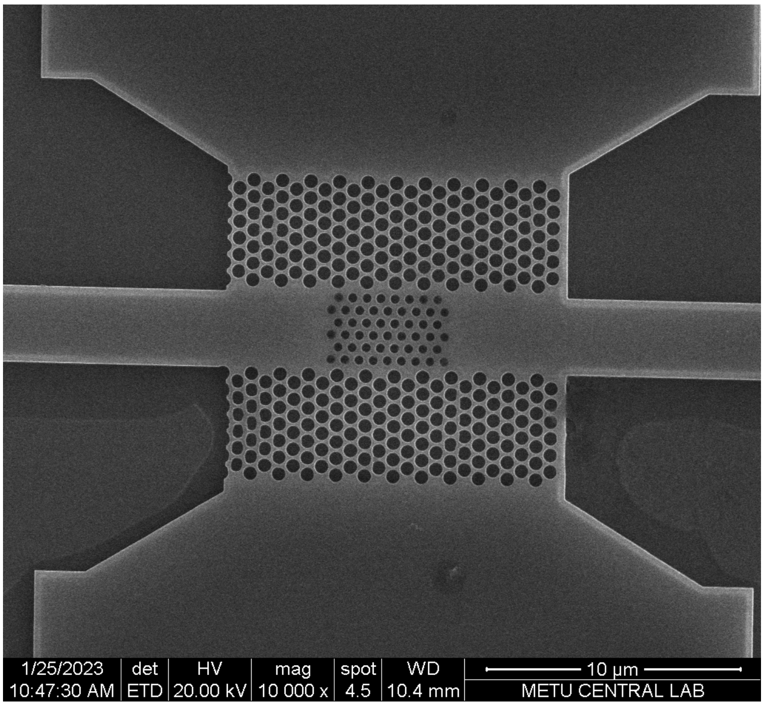

Figure 4.4: MZI active region with PhCs at Γ - K direction with side holes at Γ - M direction.

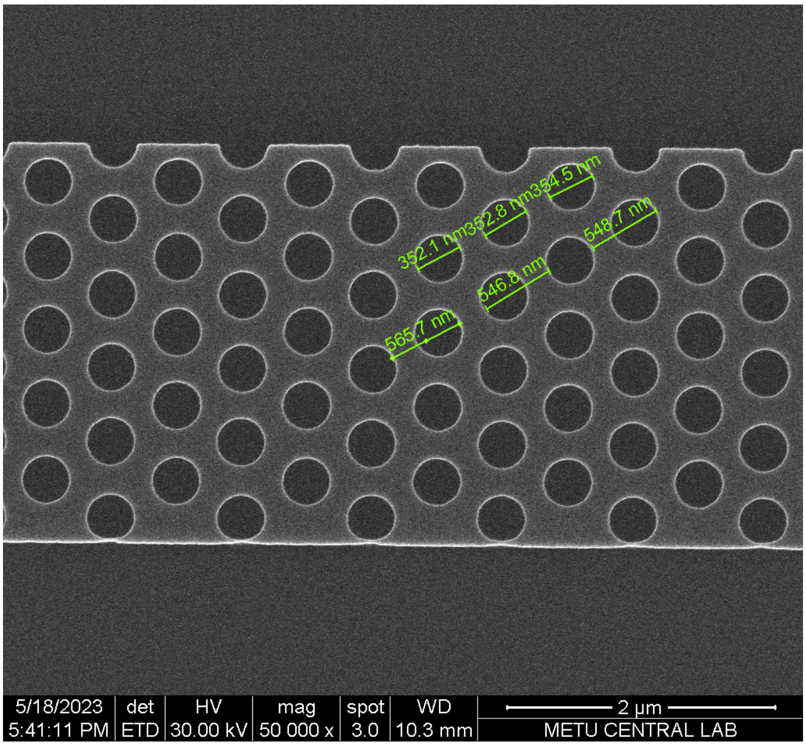

Figure 4.5: SEM imaging of photonic crystals with 310 nm design diameter at Γ - M direction (Sample 1).

we observed that the diameters of the fabricated photonic crystals are larger than the actual layout diameters, as seen in Figure 4.5. This broadening is illustrated in Figure 4.6, where the diameters of the fabricated photonic crystals are given with the error bars representing the standard deviation of the dimensions in fabrication. Similarly, the broadening of the crystal lattice period is illustrated in Figure 4.7.

The broadening of the photonic crystals causes a shift at the center wavelength of the band gap. Based on the MPB simulation results given in Chapter 3, the expected bandgaps (BGs) and the bandgap widths (BGWs) for the photonic crystals with Γ - M direction and Γ - K direction are given in Table 4.1 and Table 4.2, respectively.

As illustrated in Figure 4.6, and tabulated Table 4.1 and Table 4.2, the diameters of the photonic crystals broadened by 30-40 nm, corresponding to a bandgap shift of 30-50 nm. The effects of these shifts were considered in Section 4.2 while interpreting the results of the optical and electrical measurements. Moreover, there is approximately 5 nm broadening in the crystal lattice period, which has an insignificant effect

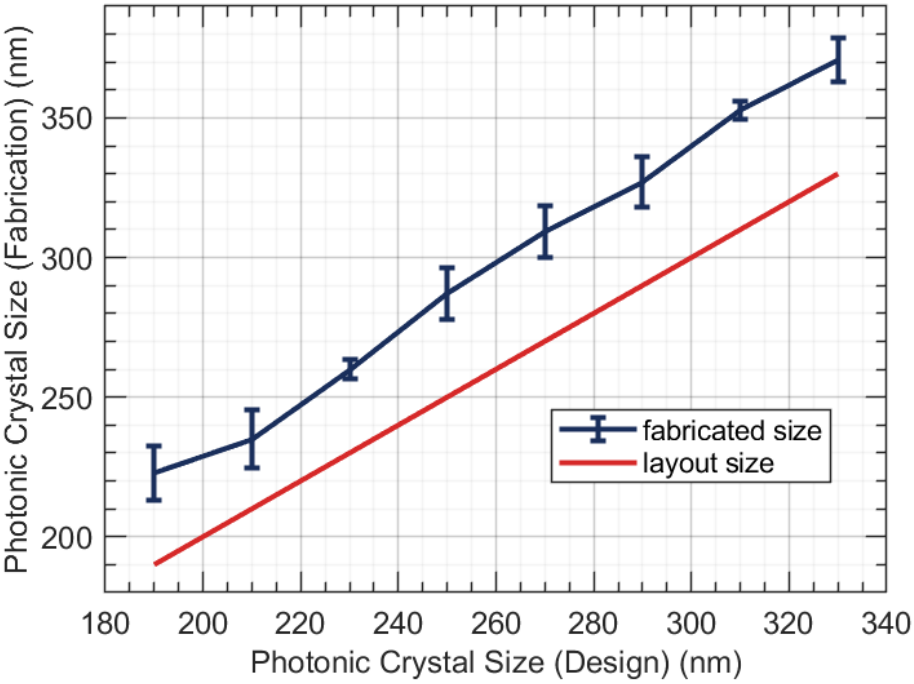

Figure 4.6: Photonic crystal size: design vs fabrication (Sample 1).

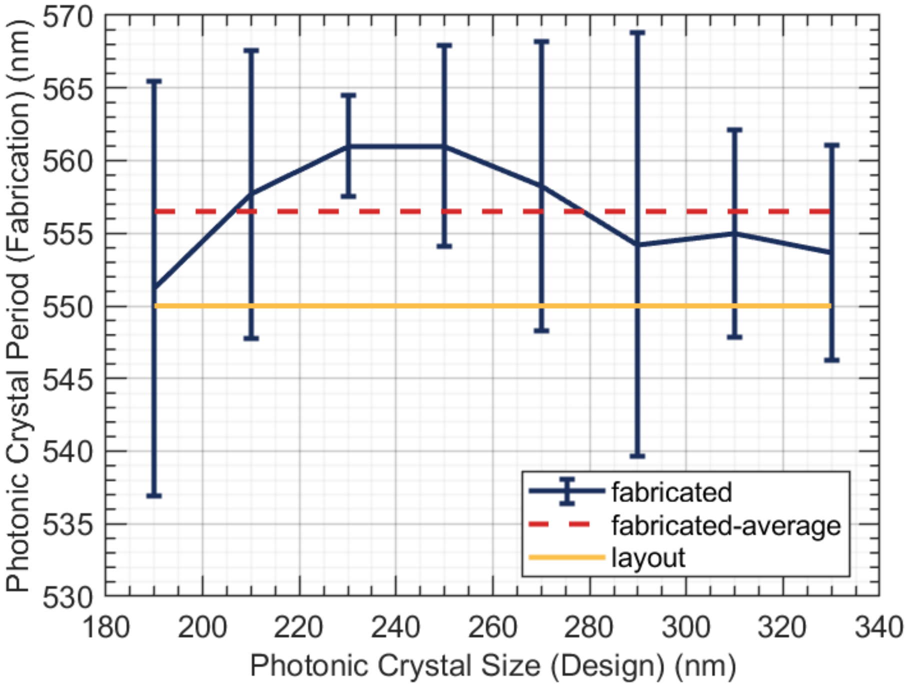

Figure 4.7: Photonic crystal period: design vs. fabrication (Sample 1).

on the band structures of the photonic crystals of interest, considering the bandgap information illustrated in Figure 3.3 and Figure 3.6.

Table 4.1: Bandgap centers (BGCs) and bandgap widths (BGWs) of photonic crystals with Γ - M direction at designed and fabricated sizes, based on MPB simulations.

Design			**Fabrication**		
D_{PhC} (nm)	BGC (nm)	BGW (nm)	D_{PhC} (nm)	BGC (nm)	BGW (nm)
270	1639.3	24.8	309.2	1599.2	14.9
290	1619.7	20.3	327.0	1578.1	9.1
310	1598.3	14.6	352.7	1544.9	0.9

Table 4.2: Bandgap centers and bandgap widths of photonic crystals with Γ - K direction at designed and fabricated sizes, based on MPB simulations.

Design		**Fabrication**	
D_{PhC} (nm)	BGC (nm)	D_{PhC} (nm)	BGC (nm)
190	1619.1	222.8	1595.5
210	1604.7	235.0	1586.7
230	1590.3	260.0	1568.7
250	1575.9	287.8	1548.0
270	1561.5	309.2	1529.8

4.2 Experimental Characterization of Modulator

Following the design and fabrication, the finished products were tested by optical and electrical measurements. The optical measurements were done by observing input and output optical powers and analyzing optical output via an optical spectrum analyzer (OSA) to observe the photonic crystal bandgaps. The electrical measurements were done by supplying electric current or voltage at electrical input ports and observing optical output ports via an oscilloscope or OSA to observe the modulator operation or shift at the output spectrum.

The photo and the simple diagram of the experimental setup are given in Figure 4.8 and Figure 4.9, respectively. The details of the setup for different measurement cases will be described in the following subsections.

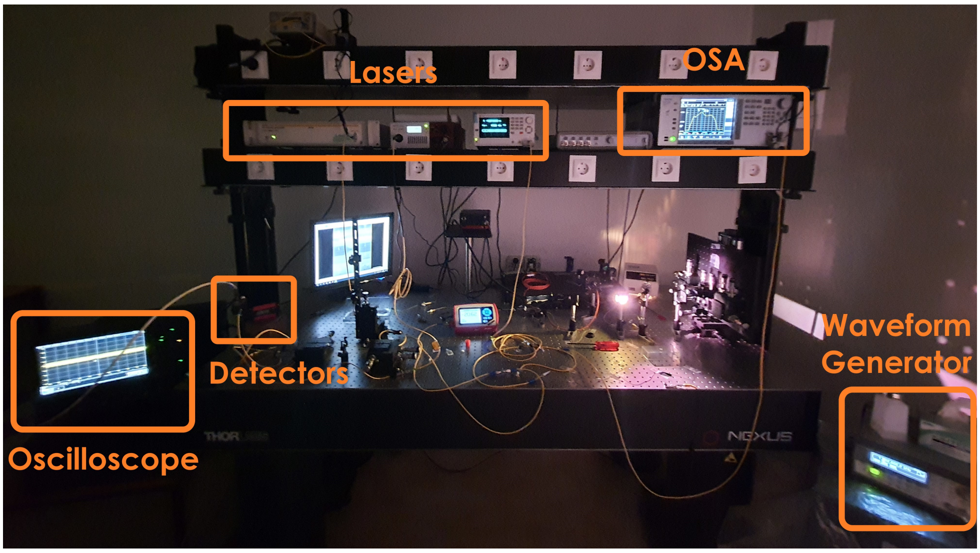

Figure 4.8: The photo of the experimental setup.

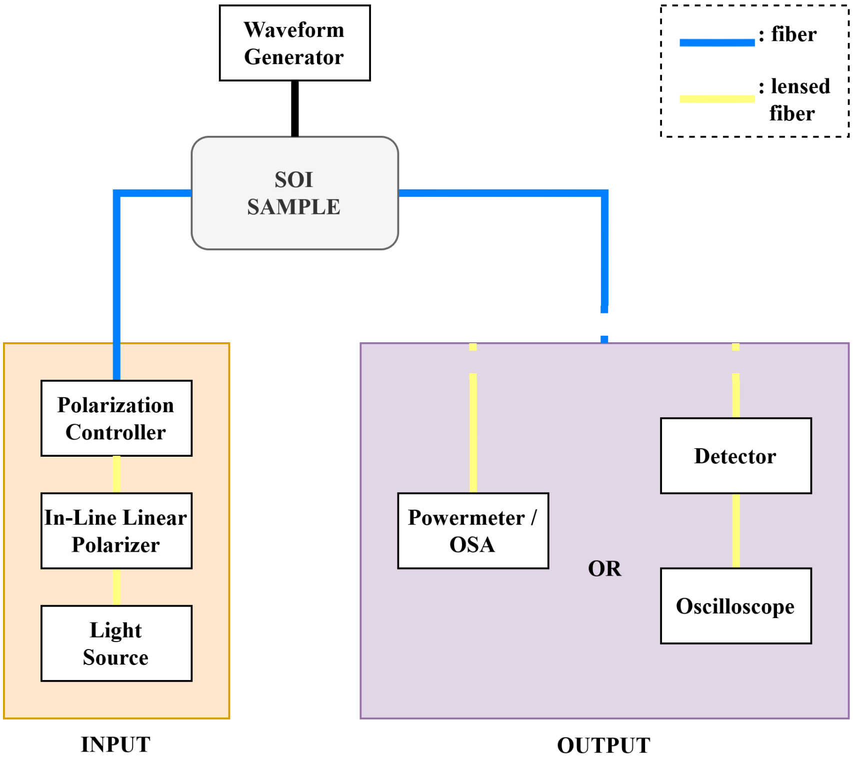

Figure 4.9: The diagram of the experimental setup.

4.2.1 Photonic Bandgap Measurements

In the experimental setup for the photonic bandgap observations, the light source Thorlabs ASE730 provides C-band and L-band light. Alternatively, the light source NKT SuperK Compact provides broadband light from 450 to 2400 nm. The input light passes through an in-line fiber polarizer (Thorlabs ILP1550SM-FC) and a three-paddle polarization controller (Thorlabs PLC-900) to adjust its polarization to TM. A single-paddle polarization controller (Thorlabs FPC031) is also used as an alternative to the three-paddle polarization controller. The TM polarized light is inputted to and outputted from the fabricated samples with tapered lensed fibers. The output light is then given to the power meter (Thorlabs S154C) or optical spectrum analyzer (Anritsu MS9740B) for optical power and transmission spectrum measurements, respectively.

The results of the bandgap measurements for photonic crystal waveguides employing 120 holes in a row with varying diameters along the Γ - M and Γ - K directions are given in Figure 4.10 and Figure 4.11, respectively.

Table 4.3: The measured bandgap centers and bandgap widths of photonic crystals with Γ - M direction with varying hole sizes.

$D_{PhC}(nm)$	Layout	270	290	310
	SEM, Sample 1	309.2	327.0	352.7
$BGC(nm)$	MPB Simulation	1599.2	1578.1	1544.9
	Sample 1	1634	1616	1587
	Sample 2	1583	1563	1539
$BGW(nm)$	MPB Simulation	14.9	9.1	0.9
	Sample 1	34	42	54
	Sample 2	46	46	50

The layout and fabricated dimensions of the photonic crystal diameters, as well as bandgap centers and the bandgap widths of both samples for Γ - M case, obtained by MPB simulations (based on SEM measurement of Sample 1) and experimental measurements of both samples, are tabulated in Table 4.3.

Examining Table 4.3, the first observation is the shift of bandgap centers by approx-

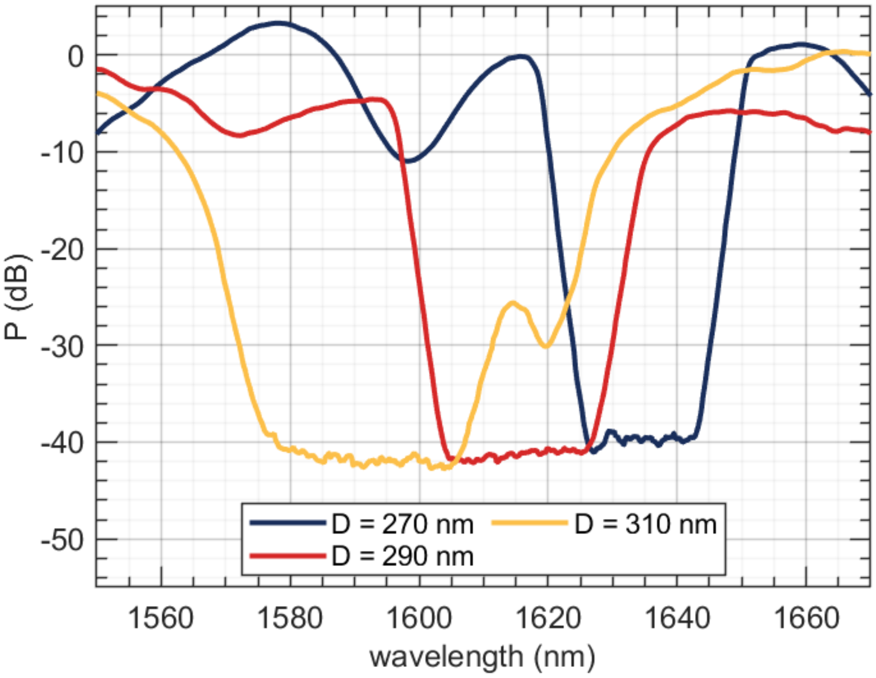

(a) Sample 1, ASE source.

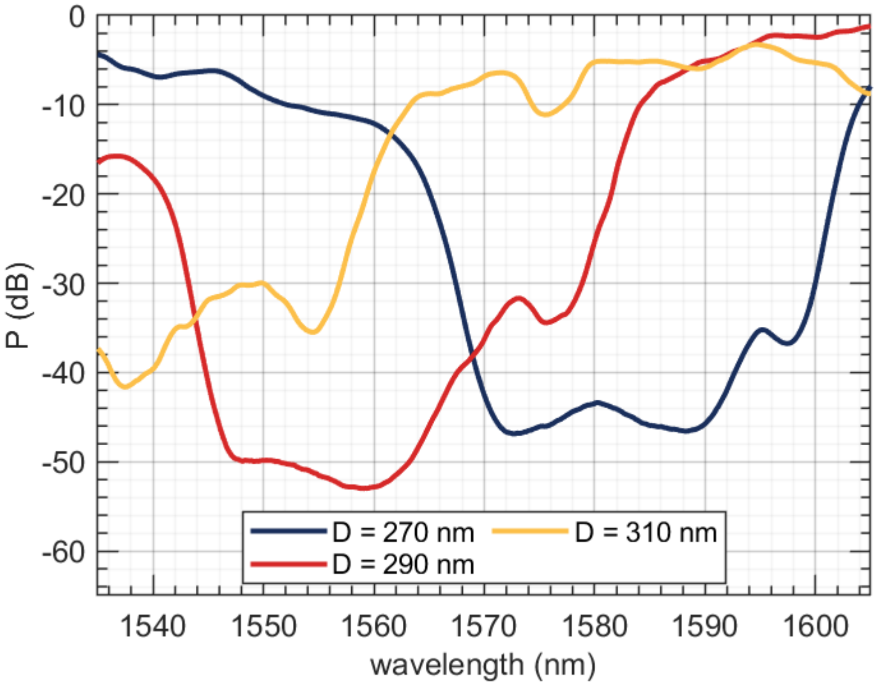

(b) Sample 2, ASE source.

Figure 4.10: The normalized spectrum of Γ - M photonic crystal waveguides with N=120.

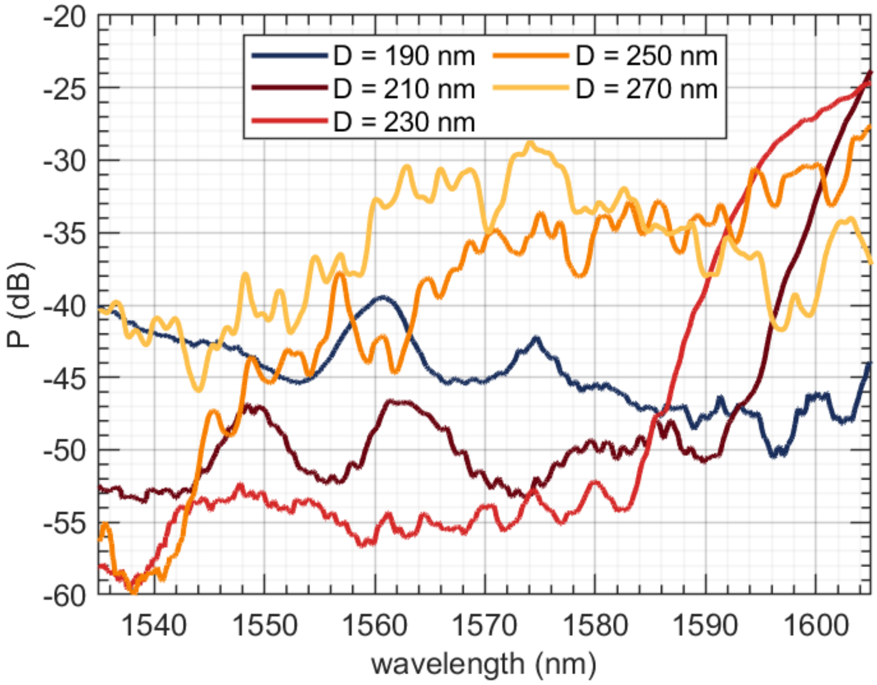

(a) Sample 1, ASE source.

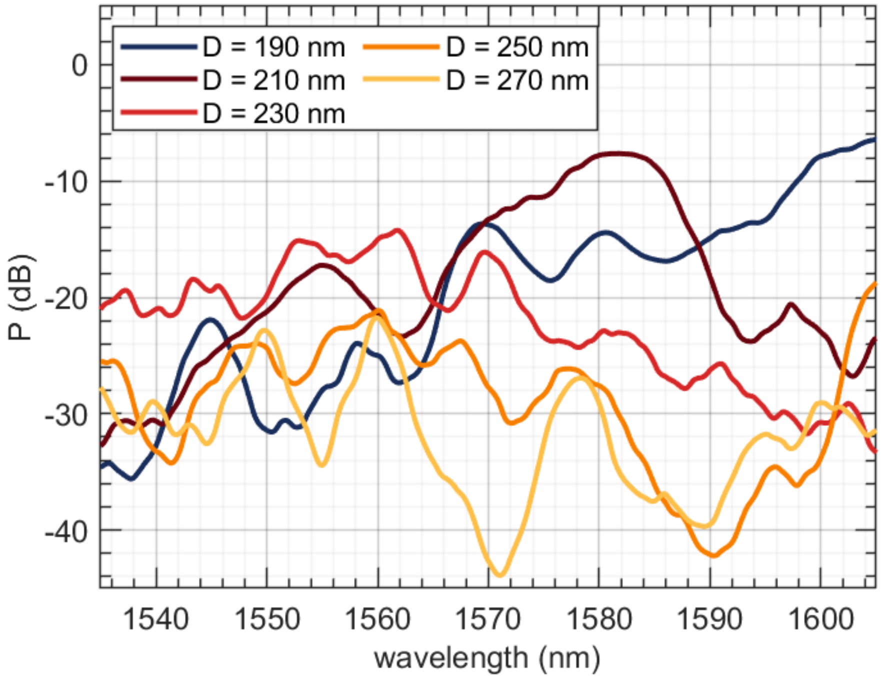

(b) Sample 2, ASE source.

Figure 4.11: The normalized spectrum of Γ - K photonic crystal waveguides with N=120.

imately 35-45 nm from the bandgap centers estimated by the MPB simulation. This might be due to computational errors of MPB, deviations in dielectric constants due to temperature differences, or errors in length measurements based on SEM images. The second observation is that there is a major uniformity problem between different samples. Although Sample 2 was not observed by SEM, an approximately 50 nm difference between measured bandgap centers indicates an approximately 40 nm difference in hole diameters between the two samples. The third observation is that the bandgap width estimation of MPB significantly deviated from the measurements.

In the case of Γ - K photonic crystals, there is no obvious bandgap in the spectrums given in Figure 4.11. Given the fact that hexagonal lattice with identical circular hole sizes have a Dirac point (cone) at the K point [29, 31, 32], not seeing a gap conforms with our expectations. Moreover, the spectrums of the Γ - K photonic crystals are highly oscillatory, and the losses at the photonic crystal regions are higher than that of Γ - M photonic crystals.

4.2.2 Verification of P-I-N Diode Operation

The current-voltage (I-V) characteristics of two of the processed PIN diodes from Sample 2 are given in Figure 4.12, where the solid line represents measured data and the dashed line represents its extrapolation. Device 1 stands for the MZI with 210 nm diameter (in layout) Γ - K photonic crystals, and Device 2 stands for the MZI with 290 nm (in layout) Γ - M photonic crystals.

Based on the I-V characteristics of the PIN diodes, it is estimated that the required 85 μA current can be achieved at around 3.5 V for both diodes.

4.2.3 Modulation Experiments

In the case of modulation experiments, the light source Santec TSL-550, which can provide single wavelength output in the wavelength range from 1500 nm to 1630 nm, is used as the light source. The waveform generator (Agilent 3322A) provides AC and DC voltage to the PIN diodes. The output light is given to a detector (Thorlabs

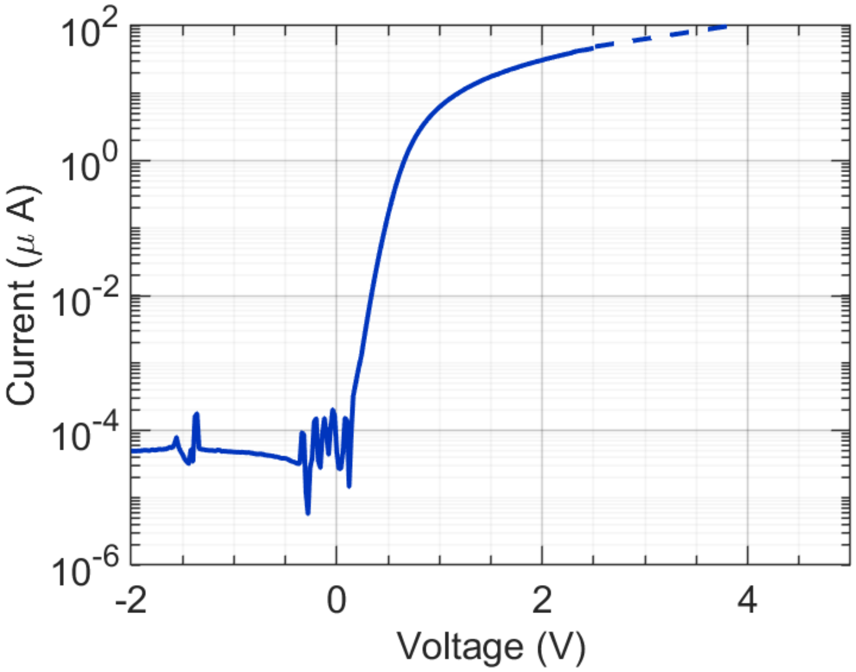

(a) Device 1.

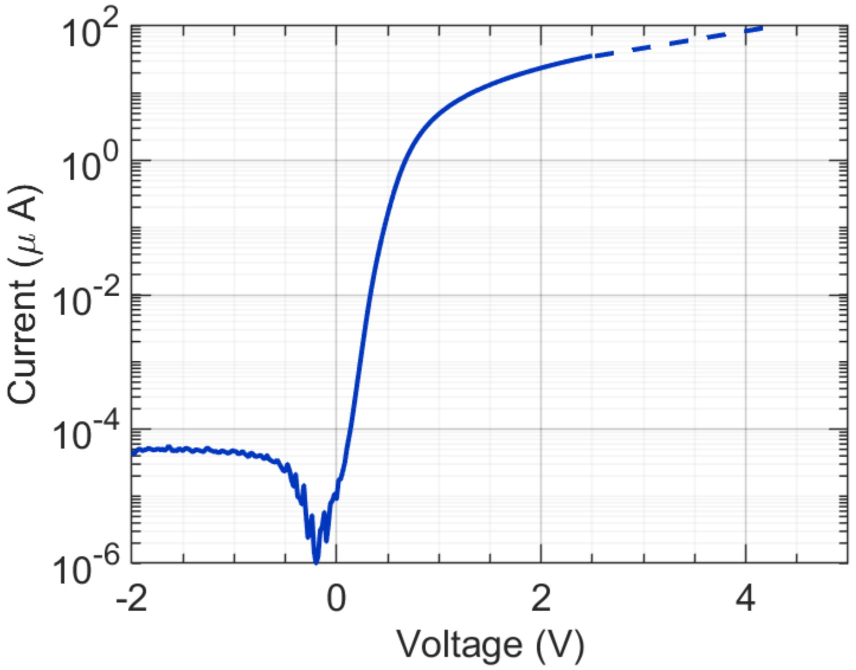

(b) Device 2.

Figure 4.12: Current-voltage characteristics of PIN diodes.

DET10N/M), and the output of the detector is then provided to the oscilloscope (Teledyne Waverunner 8404) to observe the variation of the output light intensity with time i.e. modulation operation.

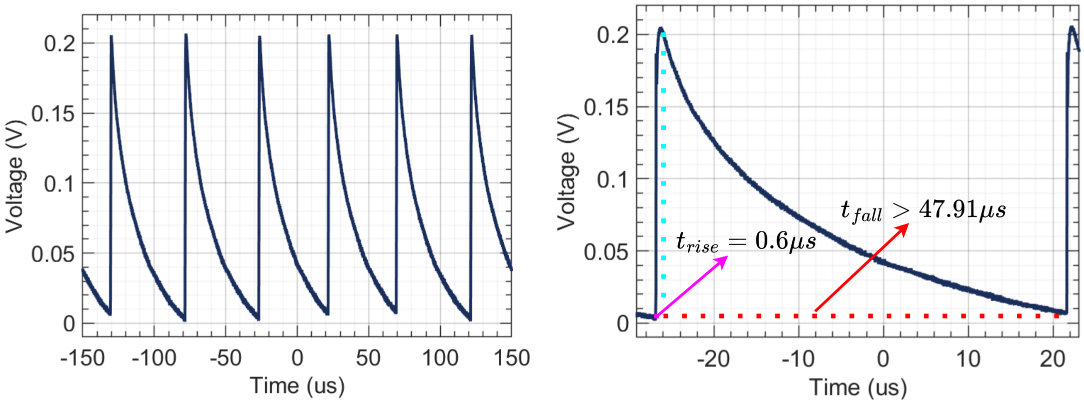

(a) 20 kHz impulse signal.

(b) Rise and fall of the signal.

Figure 4.13: Thorlabs DET10N/M, response to 20kHz impulse.

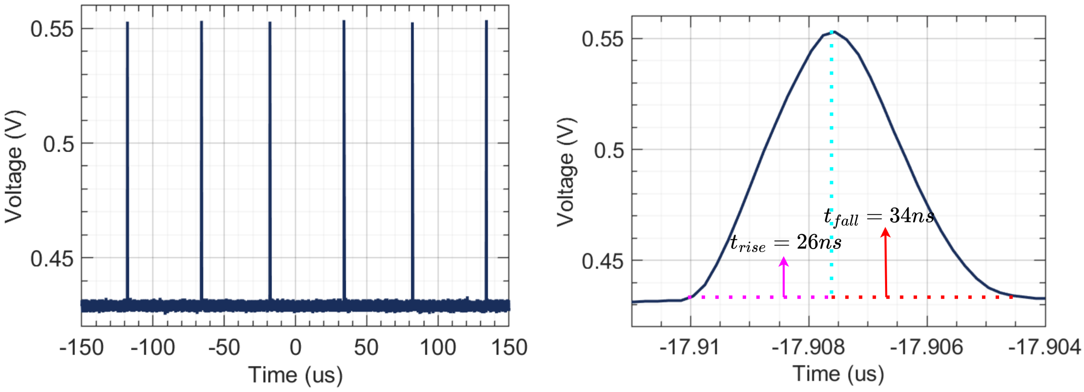

(a) 20 kHz impulse signal.

(b) Rise and fall of the signal.

Figure 4.14: Thorlabs DXM30AF, response to 20kHz impulse.

Due to current conditions in our laboratory, the detector (Thorlabs DET10N/M) is used in photovoltaic (zero-bias) mode, which suppresses the dark current but also has lower bandwidth compared to the photoconductive (reverse bias) mode [34]. The responses of our detector for time-varying input powers (a pulse signal) are given in Figure 4.13. It is seen that our detector in photovoltaic mode has rise and fall times of 0.6 and 47.9 μs, respectively. The response of another faster detector (Thorlabs

DXM30AF) is given in Figure 4.14 for comparison. For the given pulse signal, the second detector has rise and fall times of 26 and 34 ns, respectively. Unfortunately, the typical output powers of the MZIs (approximately -35 dBm) are not high enough to create a response for this detector, therefore it wasn't used in the modulation experiments. These low output powers are not expected in design and are attributed to imperfections in the fabrication steps.

Despite the bandwidth limitation of our setup, the modulation experiments were conducted to observe modulation at relatively lower frequencies. Observed waveforms on the oscilloscope for Device 1 (with photonic crystals of 210 nm diameter in layout along Γ - K direction) at the wavelength of 1551 nm are given in Figure 4.15.

Comparing Figure 4.15a and Figure 4.15b, it is seen that the modulation depth decreases as the frequency of the applied voltage increases. This might be related to the slow speed of the detector (Thorlabs DET10N/M) employed in the setup, as illustrated in Figure 4.13. Since thermal modulation also has a slow speed, it was necessary to find a way to observe waveforms at larger frequencies to eliminate the role of thermal modulation.

The examination of power spectral densities (PSDs) of waveforms observed in the oscilloscope was helpful to extend the observable frequency range. The PSDs given here were calculated by applying fast Fourier transform (FFT) to the time domain signals and converting them to frequency domain signals [35].

The single-sided PSDs of the waveforms observed on the oscilloscope for Device 1 while applying $\pm$ 5 V square wave to the one arm of the modulator at 10 kHz and 100 kHz are given in Figure 4.16a, and Figure 4.16b respectively. Similar to Figure 4.15, the modulation depth is lower at higher frequencies. Moreover, there is a clear peak at 1550 nm for the 100 kHz case.

Based on our SEM analysis and the difference between Sample 1 and Sample 2, we would expect Device 1 to have a bandgap of around 1575 nm. The 25 nm difference can be explained by non-uniformities in the fabrication process.

Although the analysis of the phase accumulation in Section 3.2.2 shows that modulation is not expected in the MZIs with photonic crystals along Γ - M direction, the same

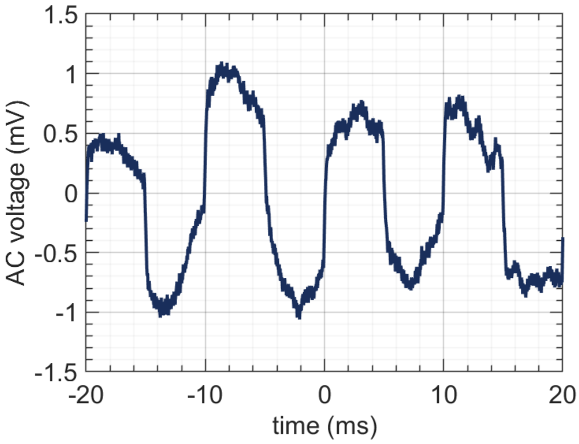

(a) f = 100 Hz, V = ± 5 V square wave.

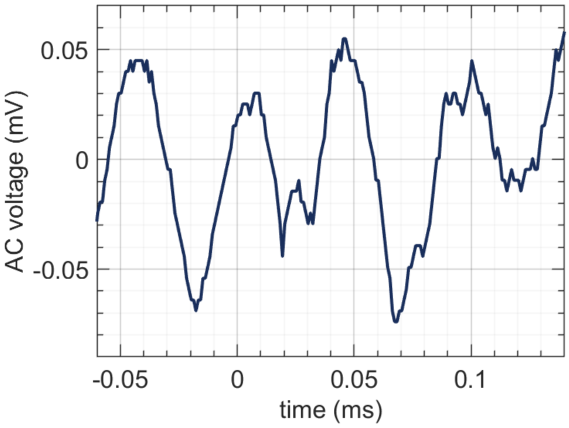

(b) f = 20 kHz, V = ± 5 V square wave.

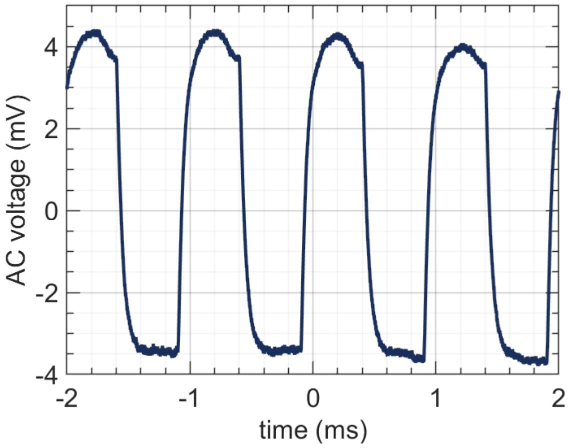

(c) f = 1 kHz, V = ± 10 V square wave.

Figure 4.15: Modulation at 1550 nm, for Device 1.

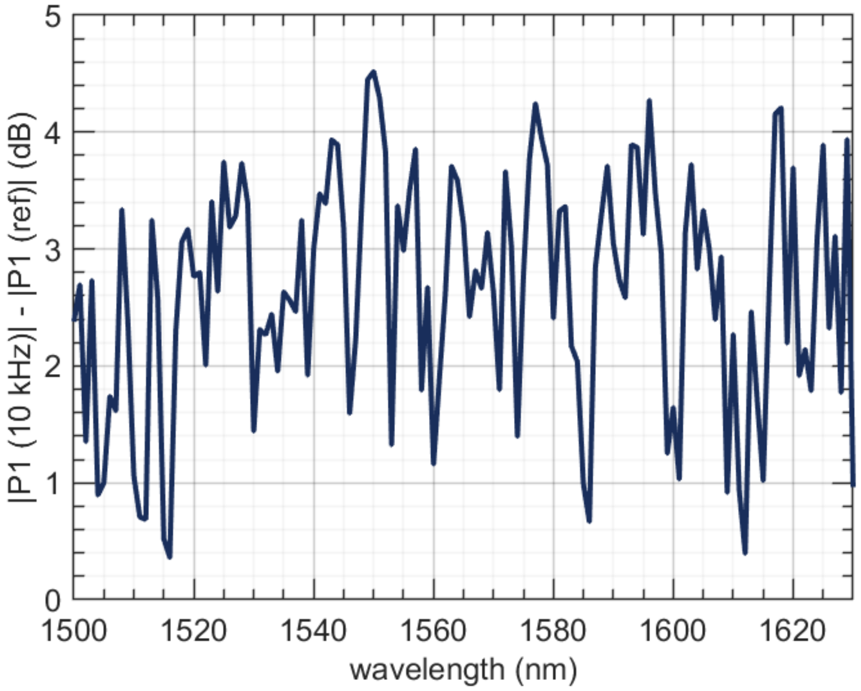

(a) f = 10kHz.

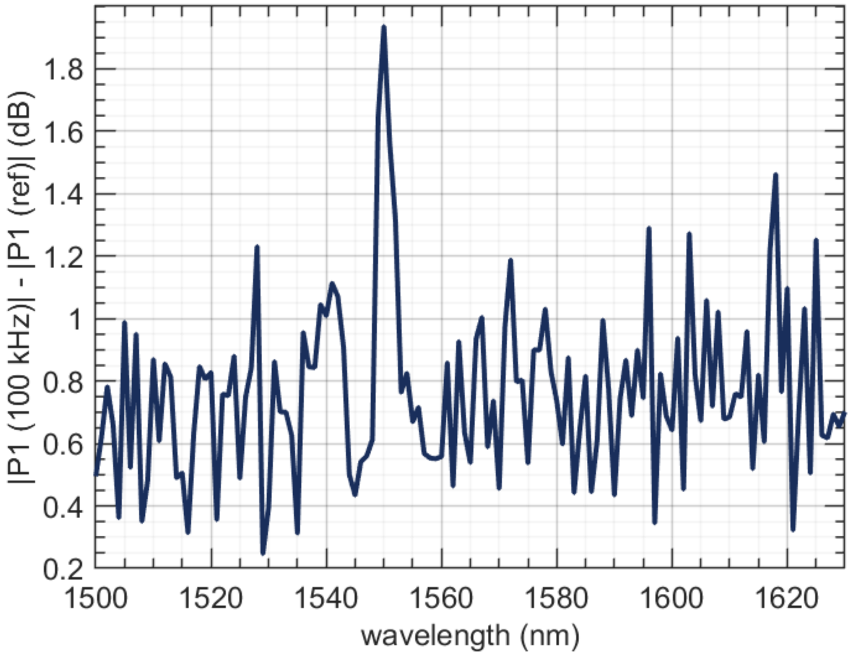

(b) f = 100kHz.

Figure 4.16: Single-sided PSD of Device 1 while applying ± 5 V square wave.

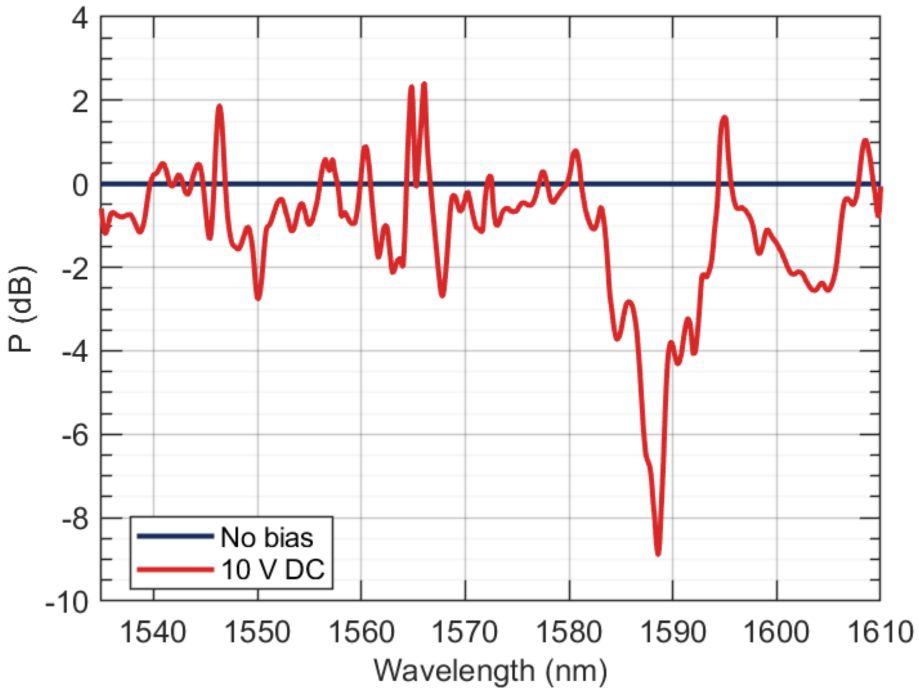

Figure 4.17: Spectrum of Device 2 while applying 10 V DC voltage.

procedures were followed for Device 2 (with photonic crystals of 290 nm diameter in the layout along Γ - M direction). When a bias voltage of 10 V DC was applied, the spectrum changed to create a minima of approximately 9 dB around 1588 nm, as seen in Figure 4.17. Here, the data corresponding to the bias case is normalized to the no-bias case. The 9 dB minima is significantly larger than all other extremum points, which correspond to less than 3 dB change. The waveguide with photonic crystals having the same dimensions has a bandgap between 1540 - 1586 nm, meaning we observed modulation at the band edge as expected.

Considering this observation, it is possible that the analysis of phase accumulation is not accurate for large bandgap photonic crystals. It should also be noted that the analysis didn't account for the effects of nonuniformities in fabrication on the band structures of photonic crystals.

CHAPTER 5

CONCLUSION AND FUTURE WORK

This thesis describes the design and experimental characterization of a photonic crystal based silicon optical modulator. Photonic crystals are useful materials employed in photonic devices thanks to the formation of photonic band structures. The operation of the designed modulator is based on the band-to-band transition to benefit from the negative refraction phenomenon and achieve large refractive index changes in comparably shorter phase shifter lengths. The band-to-band transition is achieved by utilizing PIN diodes to accumulate charges at the active photonic crystal region, changing the silicon refractive index by the plasma dispersion effect and causing a shift in the band structure.

The design steps include carefully examining photonic band structures and selecting photonic crystal parameters based on bandgap locations and widths. Moreover, an analysis of phase accumulation is provided, concluding that complete destructive interference cannot be achieved for photonic crystals at the Γ - M direction, and they are unsuitable for modulation purposes; instead, photonic crystals at Γ - K direction can be used. Based on the analysis, the number of photonic crystals in the propagation direction is selected to be 8.5, which corresponds to 4.4 μm phase shifter length. Lastly, a PIN diode design is proposed to provide a silicon refractive index change of approximately $2.7 * 10^{-3}$ via plasma dispersion effect when a current of 85 μA passes through the diode.

The experimental work entails SEM imaging of the fabricated samples, photonic bandgap measurements via observing the transmission spectrums of photonic crystal slab waveguides, and modulation experiments via applying AC and DC voltage to the diodes at the arms of the MZIs. Although there were bandwidth limitations in the experimental setup induced by the detector operating at the photovoltaic mode, the modulation operation was observed in MZI modulators using photonic crystal at both Γ - K and Γ - M directions.

Future studies may include improvements in the bandwidth of the experimental setup and repeating the modulation experiments at higher frequencies. Moreover, the modulation experiments can be repeated for more MZI modulators with varying photonic crystal parameters to better estimate the accuracy of the derived Equation 3.16 and Equation 3.17 on different scenarios. The design can be further improved by including a polarization selective device on the input side of the MZI, possibly another photonic crystal with a large TE bandgap covering the entire operation range and no TM bandgap in the operation range. Such a device would take the role of the in-line polarizer and polarization controller and simplify our experimental setup. Moreover, the proposed modulator design can be used as the building block of the design of a multiple-input and multiple-output photonic switch.

Another perspective to be considered is photonic integration, specifically the integration of III-V materials with silicon photonics. Silicon is a suitable material for electronic and passive photonic devices; however, it is indirect bandgap material and cannot effectively be used for active photonic devices. Instead, the III-V materials are efficiently used in active photonic devices. Using active III-V and passive silicon devices separately with optical interconnects leads to higher packaging costs, a larger system area, and lower power efficiency. On the other hand, the integration of silicon and III-V material systems offers a solution to these problems while bringing the benefits of the two systems together [9, 36, 37, 38, 39, 40, 41].

Our research group previously presented studies on photonic devices such as band-to-band transition based photonic crystal modulators [13, 26, 42], fano-like rod-type photonic crystal structures on bio-sensing applications [27, 43], one-dimensional slot mode photonic crystals nanobeam cavities [44, 45], amorphous photonic structures [46, 47], and nBn type InGaAs photodetectors [48, 49, 50]. Also, there is an ongoing project where the bi-functional quantum cascade lasers and photodetectors are modeled, and performance parameters for lasing and photodetection operations are evaluated. The modulator study described in this thesis and the other mentioned studies of our research group can be used as the foundation of future photonic integration studies.

REFERENCES

[1] G. Keiser, *Fiber Optic Communications*. Springer Singapore, Imprint: Springer, 2021.

[2] B. Saleh and M. Teich, *Fundamentals of Photonics*. Wiley Series in Pure and Applied Optics, Wiley, 2019.

[3] P.-J. Lin, W.-J. Ho, J.-J. Liu, C.-J. Teng, C.-C. Yu, and Y.-C. Li, "High-speed 1550-nm avalanche photodiode based on inalas-multiplicaltion and mesa-structure," in *2020 Opto-Electronics and Communications Conference (OECC)*, pp. 1–3, 2020.

[4] Y. Cheng, Y. Ikku, M. Takenaka, and S. Takagi, "Low-dark-current waveguide ingaas metal–semiconductor–metal photodetector monolithically integrated with inp grating coupler on iii–v cmos photonics platform," *Japanese Journal of Applied Physics*, vol. 55, p. 04EH01, feb 2016.

[5] D. Yin, T. He, Q. Han, Q. Lü, Y. Zhang, and X. Yang, "High-responsivity 40 gbit/s ingaas/inp pin photodetectors integrated on silicon-on-insulator waveguide circuits," *Journal of Semiconductors*, vol. 37, p. 114006, nov 2016.

[6] P. C. Eng, S. Song, and B. Ping, "State-of-the-art photodetectors for optoelectronic integration at telecommunication wavelength," *Nanophotonics*, vol. 4, no. 3, pp. 277–302, 2015.

[7] "Measuring digital development facts and figures 2021," *International Telecommunication Union*, 2021.

[8] "Measuring digital development facts and figures 2022," *International Telecommunication Union*, 2022.

[9] D. Yin, Q. Han, W. Yin, P. Feng, Q. Lv, and X. Yang, "High-responsivity ingaas/inp photodetectors integrated on silicon-on-insulator waveguide circuits,"

in *2015 14th International Conference on Optical Communications and Networks (ICOCN)*, pp. 1–3, 2015.

[10] Y. Terada, T. Tatebe, Y. Hinakura, and T. Baba, "Si photonic crystal slow-light modulators with periodic p–n junctions," *Journal of Lightwave Technology*, vol. 35, no. 9, pp. 1684–1692, 2017.

[11] R. Wu, J. Collins, D. Chekulaev, and A. Kaplan, "All-optical modulation and ultrafast switching in mwir with sub-wavelength structured silicon," *Applied Sciences*, vol. 9, no. 9, 2019.

[12] J. M and M. Jamro, *Optical Fiber Communications: Principles and Practice*. Prentice Hall Internacional series in optoelectronics, Financial Times/Prentice Hall, 2009.

[13] A. Govdeli, M. C. Sarihan, U. Karaca, and S. Kocaman, "Integrated optical modulator based on transition between photonic bands," *Scientific Reports*, vol. 8, Jan. 2018.

[14] S. J. Park, A. Zakar, V. L. Zerova, D. Chekulaev, L. T. Canham, and A. Kaplan, "All-optical modulation in mid-wavelength infrared using porous si membranes," *Scientific Reports*, vol. 6, July 2016.

[15] R. Soref and B. Bennett, "Electrooptical effects in silicon," *IEEE Journal of Quantum Electronics*, vol. 23, no. 1, pp. 123–129, 1987.

[16] G. T. Reed and C. Jason Png, "Silicon optical modulators," *Materials Today*, vol. 8, no. 1, pp. 40–50, 2005.

[17] H. Xu, X. Li, X. Xiao, Z. Li, Y. Yu, and J. Yu, "Demonstration and characterization of high-speed silicon depletion-mode mach–zehnder modulators," *IEEE Journal of Selected Topics in Quantum Electronics*, vol. 20, no. 4, pp. 23–32, 2013.

[18] T. Baba, S. Akiyama, M. Imai, N. Hirayama, H. Takahashi, Y. Noguchi, T. Horikawa, and T. Usuki, "50-gb/s ring-resonator-based silicon modulator," *Optics express*, vol. 21, no. 10, pp. 11869–11876, 2013.

[19] Y. Hinakura, Y. Terada, T. Tamura, and T. Baba, “Wide spectral characteristics of si photonic crystal mach-zehnder modulator fabricated by complementary metal-oxide-semiconductor process,” in *Photonics*, vol. 3, p. 17, MDPI, 2016.

[20] V. R. Almeida, C. A. Barrios, R. R. Panepucci, and M. Lipson, “All-optical control of light on a silicon chip,” *Nature*, vol. 431, no. 7012, pp. 1081–1084, 2004.

[21] Q. Xu, B. Schmidt, S. Pradhan, and M. Lipson, “Micrometre-scale silicon electro-optic modulator,” *nature*, vol. 435, no. 7040, pp. 325–327, 2005.

[22] J. Joannopoulos, S. Johnson, J. Winn, and R. Meade, *Photonic Crystals: Molding the Flow of Light - Second Edition.* Princeton University Press, 2011.

[23] V. Fallahi, M. Seifouri, S. Olyaee, and H. Alipour-Banaei, “Four-channel optical demultiplexer based on hexagonal photonic crystal ring resonators,” *Optical Review*, vol. 24, pp. 605–610, July 2017.

[24] H. Alipour-Banaei, F. Mehdizadeh, and M. Hassangholizadeh-Kashtiban, “A new proposal for PCRR-based channel drop filter using elliptical rings,” *Physica E: Low-dimensional Systems and Nanostructures*, vol. 56, pp. 211–215, Feb. 2014.

[25] S. G. Johnson and J. D. Joannopoulos, “Block-iterative frequency-domain methods for maxwell’s equations in a planewave basis,” *Opt. Express*, vol. 8, pp. 173–190, Jan 2001.

[26] A. Gövdeli, “Integrated optical modulators based on photonic crystals,” Master’s thesis, Middle East Technical University, 2018.

[27] S. C. Kılıç, “Two dimensional silicon photonic crystal band gap applications for optical bio-sensing and modulation,” Master’s thesis, Middle East Technical University, 2021.

[28] F. Wen, S. David, X. Checoury, M. E. Kurdi, and P. Boucaud, “Two-dimensional photonic crystals with large complete photonic band gaps in both TE and TM polarizations,” *Optics Express*, vol. 16, p. 12278, Aug. 2008.

[29] H. Chu, Y. Zhang, J. Luo, C. Xu, X. Xiong, R. Peng, M. Wang, and Y. Lai, "Band engineering method to create dirac cones of accidental degeneracy in general photonic crystals without symmetry," *Optics Express*, vol. 29, p. 18070, May 2021.

[30] C. Bradley and A. Cracknell, *The Mathematical Theory of Symmetry in Solids: Representation Theory for Point Groups and Space Groups*. Oxford Classic Texts in the Physical Sciences, OUP Oxford, 2010.

[31] T. Ochiai and M. Onoda, "Photonic analog of graphene model and its extension: Dirac cone, symmetry, and edge states," *Physical Review B*, vol. 80, Oct. 2009.

[32] M. Saba, S. Wong, M. Elman, S. S. Oh, and O. Hess, "Nature of topological protection in photonic spin and valley hall insulators," *Physical Review B*, vol. 101, Feb. 2020.

[33] Synopsys, Mountain View, CA, USA, *Sentaurus Device User Guide Version K-2015.06*, 2016.

[34] Thorlabs, USA, *DET10N(/M) Extended InGaAs Biased Detector User Guide*, 2017.

[35] R. Brown and P. Hwang, *Introduction to Random Signals and Applied Kalman Filtering with Matlab Exercises*. CourseSmart Series, Wiley, 2012.

[36] O. Marshall, M. Hsu, Z. Wang, B. Kunert, C. Koos, and D. V. Thourhout, "Heterogeneous integration on silicon photonics," *Proceedings of the IEEE*, vol. 106, no. 12, pp. 2258–2269, 2018.

[37] Y. Han, Z. Yan, W. K. Ng, Y. Xue, K. S. Wong, and K. M. Lau, "Bufferless 1.5µm iii-v lasers grown on si-photonics 220nm silicon-on-insulator platforms," *Optica*, vol. 7, pp. 148–153, Feb 2020.

[38] P. Kaur, A. Boes, G. Ren, T. G. Nguyen, G. Roelkens, and A. Mitchell, "Hybrid and heterogeneous photonic integration," *APL Photonics*, vol. 6, p. 061102, June 2021.

[39] S. Fathpour, "Emerging heterogeneous integrated photonic platforms on silicon," *Nanophotonics*, vol. 4, pp. 143–164, May 2015.

[40] Y. Xue, Y. Han, Y. Wang, Z. Zhang, H. K. Tsang, and K. M. Lau, “Bufferless III–v photodetectors directly grown on (001) silicon-on-insulators,” *Optics Letters*, vol. 45, p. 1754, Mar. 2020.

[41] D. Liang and J. E. Bowers, “Recent progress in heterogeneous III-v-on-silicon photonic integration,” *Light: Advanced Manufacturing*, vol. 2, no. 1, p. 59, 2021.

[42] A. GÖVDELİ and S. Kocaman, “Tunable integrated optical modulator with dynamical photonic band transition of photonic crystals,” vol. 10923, Conference on Silicon Photonics XIV, 2019.

[43] S. C. Kılıç and S. Kocaman, “Highly sensitive and tunable fano-like rod-type silicon photonic crystal refractive index sensor,” *IEEE Sensors Journal*, 2021.

[44] M. Erdil, “A one dimensional slot mode photonic crystal nanobeam cavity design for optical bio-sensing applications,” Master’s thesis, Middle East Technical University, 2020.

[45] M. Erdil and S. Kocaman, “Optomechanically enhanced high-q slot mode photonic crystal nanobeam cavity,” 31st Annual IEEE Photonics Conference (IPC) of the IEEE-Photonics-Society, 2018.

[46] M. C. Sarıhan, “Photonic integrated circuit components with amorphous structures,” Master’s thesis, Middle East Technical University, 2018.

[47] M. C. Sarihan, Y. B. Yilmaz, M. Erdil, M. S. Aras, C. Yanik, C. W. Wong, and S. Kocaman, “Flexible waveguides with amorphous photonic materials,” vol. 10914, 2019.

[48] A. Şahin, “Optimization, fabrication, and characterization of dual-band ingaas nbn photodetectors,” Master’s thesis, Middle East Technical University, 2022.

[49] F. Uzgur, “Barrier engineering for high-performance nbn infrared photodetectors,” Master’s thesis, Middle East Technical University, 2020.

[50] A. Şahin, M. S. Gül, F. Uzgur, and S. Kocaman, “Dual-band ingaas nbn photodetectors at 2 mu m,” *APPLIED PHYSICS LETTERS*, vol. 120, no. 9, 2022.